

# Grain size distribution in protoplanetary disks

*Erik Dahlöf*

---

Lund Observatory  
Lund University



2016-EXA106

Degree project of 15 higher education credits  
June 2016

Supervisor: Bertram Bitsch

Lund Observatory  
Box 43  
SE-221 00 Lund  
Sweden

---

## Abstract:

Protoplanetary disks consist of matter in both gas and solid form. The sizes of the solid particles, dust grains, although in minority compared to the gas, are important in the formation of larger bodies such as planetesimals. This is a topic which has been widely explored. However, the impact of the dust grain sizes on the underlying disk structure has not yet been as extensively modeled. Different sizes of dust grains are often disregarded.

Dust particles are the main contributors to the opacity of a protoplanetary disk and thus have a great impact on the disk temperature. This is due to the cooling rate dependence on opacity. The aims of this work is to, first model a dust size distribution in a protoplanetary disk, and second, calculate the new mean opacity of the disk due to the size distribution.

Birnstiel et al. (2011) provides a recipe for simulating dust size distributions in protoplanetary disks numerically. The input parameters for the recipe are taken from the disk structures provided by Bitsch et al. (2015). These disks use only  $\mu m$  sized grains for opacity calculations (Bell & Lin 1994). The result is grain size distributions for the considered disk structures.

The RADMC 3D code provided by Dullemond is used to calculate the mean opacity of the grain size distributions.<sup>1</sup> The resulting mean opacity is compared to the Bell & Lin (1994) opacity used in the Bitsch et al. (2015) disk structures.

The temperature, surface density and scale height parameters are fully determined by the disk structure. However, the fragmentation velocity of grains, the metallicity and the turbulent strength of the disk, have certain ranges of allowed values in a protoplanetary disk. The mean opacity is comparable to the Bell & Lin (1994) opacity only for a very specific parameter space. This indicates that the  $\mu m$  grain approximation is, in most cases, not very good.

---

<sup>1</sup><http://www.ita.uni-heidelberg.de/dullemond/software/radmc-3d/>

---

## Populärvetenskaplig beskrivning

Uppkomsten av solsystemet, dess planeter och andra himlakroppar har länge varit ett aktivt forskningsområde för astronomer. Grunden till den aktuella teorin om planetformation lades redan i mitten på 1700-talet av Immanuel Kant. Den beskriver hur planeter formas i en disk av gas och fasta partiklar kretsandes kring den centrala, unga Solen, en så kallad solar nebula, eller protoplanetarisk disk. Kant noterade att alla planeter i solsystemet kretsar kring Solen i samma rotationsplan samt har samma rotationsriktning. Dessa fakta pekar på att planeterna i solsystemet har ett gemensamt ursprung. Sedan 1700-talet har forskare byggt på och utvecklat den ursprungliga modellen till den, vidspredda, modellen som nu är generellt accepterad. Sedan slutet av 1900-talet har många exoplaneter, tillhörande andra stjärnor än solen, påvisats. Solar nebula teorin anses, därför, vara ett steg i evolutionen för de flesta stjärnor i Universum.

Solar nebula teorin är baserad på den generella teorin bakom stjärnformation. Stjärnor bildas i extremt stora moln av gas och fasta partiklar. Molnen är massiva nog att dras ihop av egen gravitation och under kontraktionen uppkommer punkter av skiftande densitet. Punkter med hög densitet drar till sig mer materia och blir mer och mer massiva. Tryck, temperatur och densitet ökar stadigt i dessa punkter tills det blir tillräckligt för att starta fusions reaktionerna som definierar stjärnor. De nyformade stjärnorna är omringade av molnet som de skapades ur och de fortsätter att dra till sig materia. Rotation av stjärnorna leder till att gas och fasta partiklar ansamlas i en rotations-disk, en protoplanetarisk disk.

Disken har till en början extremt hög temperatur, densitet och högt tryck. Allt eftersom den centrala stjärnan drar till sig mer materia så svalnar disken och får lägre densitet och tryck. Det leder till att fler och fler element kondenserar till sin fasta form och kan bilda mer komplexa partiklar. De fasta partiklarna är viktiga för formandet av planeter och andra himlakroppar och därmed är även strukturen på disken viktig, dvs. temperaturen, densiteten etc.

Simulationer av struktur i protoplanetariska diskar är viktiga då observationer av dessa diskar är svåra av flera anledningar. Diskarna ofta insvepta i de stora gas och partikel moln som bildat stjärnorna vilket gör dem gömda från sikt. Dessutom existerar de protoplanetariska diskarna under kort tid, sett ur en stjärnas perspektiv, vilket gör att de är sällsynta i stjärnhimlen.

# Contents

<b>1</b>	<b>Introduction</b>	<b>3</b>
<b>2</b>	<b>Method</b>	<b>8</b>
2.1	Coagulation/fragmentation . . . . .	8
2.1.1	Coagulation . . . . .	8
2.1.2	Fragmentation . . . . .	10
2.2	Size regions . . . . .	12
2.2.1	Relative velocity regions . . . . .	12
2.2.2	Settling effects . . . . .	15
2.2.3	Grain size regimes . . . . .	16
2.3	Simulations . . . . .	17
2.3.1	Fragmentation and cratering . . . . .	17
2.3.2	Grain size distribution . . . . .	18
2.4	Opacity . . . . .	21
2.4.1	Midplane density . . . . .	22
2.4.2	Weighted mean opacity . . . . .	24
2.5	Radial drift . . . . .	25

<b>3 Results</b>	<b>28</b>
3.1 Grain size distribution . . . . .	28
3.2 Opacity . . . . .	34
<b>4 Conclusions</b>	<b>36</b>
<b>5 Appendix</b>	<b>40</b>
5.1 Appendix A: Sequential growth . . . . .	40
5.2 Appendix B: Fragmentation velocity . . . . .	41
5.3 Appendix C: Deadzone simulation . . . . .	42

# Chapter 1

## Introduction

Stars are thought to form in great interstellar clouds of gas and dust. Gravitational perturbations cause the cloud to slowly collapse into points of higher density. This causes pressure, temperature and density of these points to increase which leads to more rapid accretion. Eventually young stars are formed in these points.

Asymmetries in the mass accretion, as well as the initial angular momentum of the cloud, leads to rotation of the system which results in a rotational disk forming around the star. A protoplanetary disk consists of "leftover" material from the newly formed star. This is a mixture of hydrogen and helium. More massive elements are also present in the disk but are very scarce. These are called metals. The atoms and molecules are by majority in gas form. The disk starts out as very dense and hot but as the young central star continues to accrete mass, both the density and the temperature drop. The decreasing temperature causes elements to condense and more solids are created. These solids form porous dust grains of very low internal density, mainly silicates and water ice. The dust grains will be the focus of this article.

The structure of a protoplanetary disk is a complex system which depends on several parameters. The matter of the inner protoplanetary disk is, due to turbulent viscosity, constantly losing angular momentum to the far outer parts of the disk. This causes the matter of the inner disk to migrate towards the central star, while the far outer disk moves outwards. For the purpose of this work, only the part of the disk with inward motion is considered. The inward flux of mass in the inner disk is denoted  $\dot{M}$ . The viscosity of the disk is low and the accretion process takes millions of years. As the structure of the disk changes, so does the viscosity and thus also the accretion rate. Different accretion rates define different epochs, or ages, of the disk. Old protoplanetary disks have low mass accretion rates while young disks accrete mass more quickly.

The viscosity,  $\nu$ , at a given orbital distance in the disk is given by the temperature,  $T$ , and the local keplerian rotational frequency,  $\Omega_K$ .

$$\nu = \alpha_t \frac{c_s^2}{\Omega_K} \quad (1.1)$$

This is the alpha-viscosity (Shakura & Sunyaev 1973) approach where  $\alpha_t$  determines the turbulent strength. The temperature enters through the speed of sound  $c_s = \sqrt{\frac{kT}{\mu m_p}}$ , where  $k$  is Boltzmanns constant,  $\mu$  is the mean molecular weight and  $m_p$  is the proton mass.

The viscosity determines the inward velocity of matter,  $v_r = -\frac{3\nu}{2R}$  where  $R$  is the orbital distance. The mass accretion is described by Lynden-Bell & Pringle (1974):

$$\dot{M} = -2\pi R \Sigma v_r \quad (1.2)$$

Here,  $\Sigma$  represents the vertically integrated density of the disk, the surface density. By inserting  $v_r$  into the equation above one obtains:

$$\dot{M} = 3\pi\alpha_t H^2 \Omega_K \Sigma \quad (1.3)$$

Where  $H = \frac{c_s}{\Omega_K}$  is the scale height of the disk. It is a parameter determining the vertical extension of matter from the mid plane. The protoplanetary disk is assumed to be in a steady state and thus  $\dot{M}$  must be constant over all radii  $R$ . Therefore any changes in the parameters  $\Sigma$ ,  $H$ ,  $T$  or  $\alpha_t$  must be compensated by the others ( $\Omega_K$  is only dependent on  $R$  and the mass of the central star).

It becomes clear from the constant  $\dot{M}$  above that the three parameters  $T$ ,  $H$  and  $\Sigma$  are important for determining the structure of the protoplanetary disk. They are all dependent on each other and vary with  $R$  which complicates the task.

The temperature of the disk is mainly determined by three processes, viscous heating  $Q^+$ , stellar heating  $S^+$  and radiative cooling  $Q^-$  (Bitsch et al. 2013). The equilibrium between the three processes can be expressed as  $Q^+ + S^+ = Q^-$ .

The viscosity of the disk leads not only to the mass accretion, but also to frictional heating given by Dullemond (2013):

$$Q^+ = \Sigma \nu \left( R \frac{d\Omega_k}{dR} \right)^2 \quad (1.4)$$

The heating is thus proportional to  $\Sigma$ ,  $\nu$  and  $\Omega_K$ . By equation 1.1 and 1.2,  $\nu$  and  $\Sigma$  are inversely proportional if  $\dot{M}$  is constant. However, since  $\Omega_k$  grows inwards in the disk,

$Q^+$  is dominating at small  $R$ . Even though the viscosity is small, the heating provided is significant.

The irradiation of the disk by the central star provides another source of heat,  $S^+$ . Because of the opacity of the gas and dust grains, the disk absorbs incoming radiation. The absorption leads to increased energy and thus increased temperature. The intensity of the stellar irradiation at different locations of the disk is highly dependent on the shape of the disk,  $H$ . However,  $H$  itself is dependent on temperature as seen above which makes the problem complex. The stellar heating is proportional to the flux from the central star  $F_*$  and the projected angle onto the disk surface. As can be seen below,  $H$  is usually a growing function with  $R$  and thus the stellar heating dominates further out in the disk. The depth at which most of the radiation is absorbed is given by the radial and vertical opacity structure and thus the optical depth. At locations where the opacity is large, the disk is opaque and all incoming radiation is absorbed. At locations where the opacity is small the disk is more transparent and the stellar irradiation is absorbed in deeper layers.

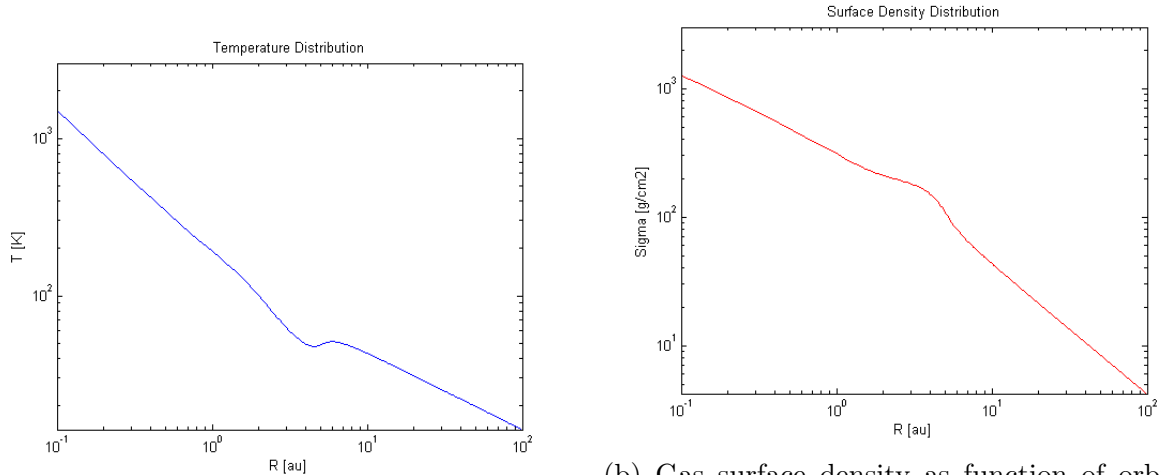
The radiative cooling rate  $Q^-$  is the rate at which energy is emitted, transported within and radiated away from the disk. It is heavily dependent on the density and opacity of the disk.

$$Q^- \propto \frac{1}{\rho\kappa} \quad (1.5)$$

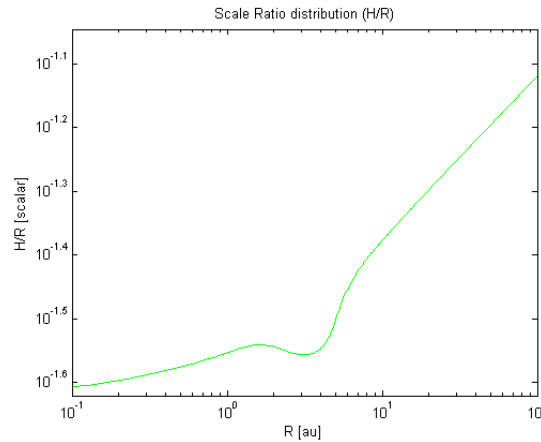
A large cooling rate means that the disk cools off quickly and most likely has a low temperature in its steady state as a result.

Simulations of the structure of protoplanetary disks have been carried out, for example in Bitsch et al. (2015). In the simulations an initial  $\Sigma(R)$  is assumed. The three heating processes and the disk opacity lead to a  $T(R)$  structure in the disk which in turn leads to a  $H(R)$  structure,  $T \propto \left(\frac{H}{R}\right)^2$ . The  $H(R)$  structure changes the viscosity  $\nu$  and thus  $\Sigma$ ,  $T$  and  $H$  have to be re-evaluated. This process is repeated until an equilibrium state is found. This is a simplified version of the actual simulations. The resulting structure of the disk parameters can be seen in figure 1.1. Both  $T$  and  $\Sigma$  decrease with larger  $R$  while  $H/R$  increases. All of the parameters feature a bump at  $R \sim 2au$ . This bump is due to the transition of water ice into vapor, at  $T \sim 180K$ . Water ice has larger opacity than vapor, which results in a slower cooling rate at large  $R$ . Slower cooling rate means increased  $T$  which in turn leads to a larger  $H/R$  and a smaller  $\Sigma$ . The increased scale height means that the stellar heating,  $S^+$ , has greater effect on the disk beyond the ice line. This increases  $T$  and  $H/R$  even further and causes the flaring appearance of the disk. The sudden bump in  $H/R$  at the ice line causes the outward neighboring part of the disk to be shadowed from stellar heating and thus  $T$  in this small region is slightly decreased. This can be seen as a small dip in  $T$  and  $H/R$  at  $R \sim 2$  in figure 1.1. The structure is complicated by the decrease in  $\Sigma$  at the ice line. Due to equation 1.5 a decrease in density leads to larger cooling rate which somewhat counteracts the arguments

above. This reflects the complexity of the parameter space.



(a) Temperature as function of orbital distance. (b) Gas surface density as function of orbital distance.



(c) Scale height as function of orbital distance.

Figure 1.1: Disk structure of the 1 Myr epoch. Bitsch et al. (2015) simulated temperature, surface density and scale height of a protoplanetary disk using hydrodynamical codes. The three heating processes,  $Q^+$ ,  $S^+$  and  $Q^-$ , were incorporated into the simulations along with a  $\mu m$  grain size distribution.

As mentioned, the matter of a protoplanetary disk is dominated by gas. The exact concentration of solids,  $\Sigma_d$ , is difficult to determine but it can be approximated as a few percent of the gas surface density,  $\Sigma_g$ .

The dust grains in a protoplanetary disk grow by collisions and, subsequently, sticking to other dust grains. Due to turbulence and random motions of the gas in the disk the dust grains obtain relative velocities. A dust grain typically starts out as very small, smaller than  $\mu m$ . Such small grains are easily coupled to the motion of the gas in the disk and have low relative velocities (see section 2.2.1). This enables the sticking of small dust grains to

form larger ones. This process is called coagulation. The coagulation leads to larger dust grains which eventually become enough to decouple from the gas and gain larger relative velocities (see section 2.2.1). At a certain grain size the relative velocities will be large enough for collisions to result in bouncing, cratering and fragmentation. Fragmentation leads to redistribution of fragments to all grain sizes.

These two processes, coagulation and fragmentation, lead to an equilibrium state of the dust sizes, a size distribution. The dust distribution is mainly determined by the disk structure parameters defined above:  $T$ ,  $\Sigma$ ,  $H$ ,  $\alpha_t$  and, as we will see later, the fragmentation velocity,  $u_f$ , and the metallicity,  $Z$ .

The size distribution of dust in a protoplanetary disk is important to understand for several reasons. First off, high concentrations of large grains in close vicinity can lead to a self gravitating system which produces planetesimals, the first step towards planetary formation. Such a high concentration of particles in a part of the protoplanetary disk can be achieved by the streaming instability.

Furthermore, dust grains are the main contributors to the opacity of the protoplanetary disk. The opacity directly determines the cooling rate of the disk by equation 1.5, that is the rate at which radiation escapes the disk. The opacity also determines the depth at which most of the stellar irradiation is absorbed. This means that the opacity affects the overall temperature, which then determines the whole structure of the disk.

The result of the simulations described above (Bitsch et al. 2015) are distributions of  $T$ ,  $H$  and  $\Sigma_g$  for various  $R$  and ages of the disk ( $M$ ). Note that  $T$  from these simulations is the midplane temperature. In the simulations the opacity of the dust grains has been included. However, for simplicity all of the dust grains in the disk were assumed to be of the same size ( $\mu m$ ). The goal of this work is to simulate a realistic, steady state dust size distribution, derived from the parameters  $T$ ,  $H$ ,  $\Sigma_g$ ,  $R$  and  $\alpha_t$  obtained from the simulations by Bitsch et al. (2015). The dust distribution is used to calculate the mean opacity at all  $R$  of the disk. The mean opacity is then compared to the Bell & Lin (1994) opacity profile used in the disk structure simulations.

# Chapter 2

## Method

### 2.1 Coagulation/fragmentation

As described above the dust grains in a protoplanetary disk are in a steady state size distribution caused by the coagulation and fragmentation processes. Below, the physical model of this steady state will be described as well as the code used to calculate it. It is important to note that in reality there are two factors determining the upper mass threshold of the grains, fragmentation and radial drift. For the purposes of this work, only fragmentation at a certain particle mass will be considered as this limit. This approach will be justified later on in section 2.5.

#### 2.1.1 Coagulation

For simplicity, a smallest mass of grains  $m_0$  is used as lower mass limit. The fragmentation mass limit is  $m_f$ , above which all grains are fragmented in collisions. This limit on the upper mass of grains is actually set by the fragmentation velocity. Colliding particles have relative velocity to each other. Above a certain relative velocity,  $u_f$ , the grains fragment upon collision. The relative velocity of grains in a protoplanetary disk is mainly determined by turbulence and Brownian motion, which are both dependent on the mass and size of the grains (see section 2.2.1). This links the fragmentation velocity,  $u_f$ , directly to a fragmentation mass,  $m_f$ . The masses  $m_0$  and  $m_f$  thus limit the grain mass distribution in this model. Considering the grains to consist mainly of water ice and silicates, the value of  $u_f$  ranges between 1 – 10  $m/s$  (Gundlach & Blum 2015).

First off, a collision kernel is introduced. The collision kernel defines the number of collisions per unit time per unit volume between masses in two intervals around  $m_1$  and

$m_2$ . By Birnstiel et al. (2011) the collision kernel has the following form:

$$C_{m_1, m_2} n(m_1) n(m_2) dm_1 dm_2 \quad (2.1)$$

With:

$$C_{m_1, m_2} = m_1^v h \left( \frac{m_2}{m_1} \right) \quad (2.2)$$

From Tanaka et al. (1996).  $v$  is the index of the kernel. It is an important parameter for describing the collisions of dust in the disk.

Here,  $n(m)$  is the number density of particles. By Birnstiel et al. (2011) it is described as a power law of the dust grain mass. The exponent  $\alpha_c$  is central for the dust distribution and will be described further below.

$$n(m) = A m^{-\alpha_c} \quad (2.3)$$

$A$  is a constant of proportionality. The  $h$  function, which defines the kernel, has the following power law dependence (Makino et al. 1998):

$$h \left( \frac{m_2}{m_1} \right) = h_0 \begin{cases} \left( \frac{m_2}{m_1} \right)^\gamma & \text{for } \frac{m_2}{m_1} \ll 1 \\ \left( \frac{m_2}{m_1} \right)^{v-\gamma} & \text{for } \frac{m_2}{m_1} \gg 1 \end{cases} \quad (2.4)$$

$\gamma$ , together with  $v$ , determines the collision probability of the dust grains. The number of collisions per unit volume per unit time is thus determined by  $\alpha_c$ ,  $v$  and  $\gamma$ .

As explained in the introduction, collisions between grains leads to coagulation which results in bigger grain sizes. This can be thought of as a flux of mass from small sizes to bigger sizes,  $F(m)$ . The total mass of the system is assumed to be conserved:

$$\frac{\partial mn(m)}{\partial t} = - \frac{\partial F(m)}{\partial m} \quad (2.5)$$

As the particles grow to the fragmentation mass  $m_f$  they obtain large enough velocities to fragment and redistribute to smaller masses. In a protoplanetary disk a steady state of coagulation/fragmentation is assumed. For a steady state  $\frac{\partial mn(m)}{\partial t} = 0$ . This makes  $F(m) = \text{constant}$ .

The flux of mass can be described by an integration of the number of collisions per time unit per volume over all masses (Birnstiel et al. 2011):

$$F(m) = \int_{m_0}^m dm_1 \int_{m-m_f}^{m_f} dm_2 m_1 C_{m_1, m_2} n(m_1) n(m_2) \quad (2.6)$$

By substituting the collision kernel from equations 2.2 and 2.3 and using the flux constancy one arrives at:

$$F(m) \propto m^{v-2\alpha_c+3} = \text{constant} \rightarrow \alpha_c = \frac{v+3}{2} \quad (2.7)$$

This is regardless of the form of equation 2.4 as can be seen in Tanaka et al. (1996). The  $\gamma$  parameter can therefore be disregarded. This  $\alpha_c$  can then be used in equation 2.3 to calculate the number density of particles at a certain mass. Then by assuming a constant grain porosity, the size number density can be readily obtained by:

$$m = \frac{4\pi}{3} \rho_s a^3 \quad (2.8)$$

Where  $\rho_s$  is the density of material in a grain and  $a$  is the grain size (grain radius). The steady state of mass flux described by equation 2.5 requires a constant resupply of mass. So far, this model considers only resupply of monomers,  $m_0$ , but no resupply of any other grain masses. This is unrealistic and the next section also takes fragmentation into account.

### 2.1.2 Fragmentation

At  $m_f$  all grains are assumed to fragment into smaller grain masses at a rate (Birnstiel et al. 2011):

$$\dot{n}_f(m) = Nm^{-\xi} \quad (2.9)$$

$\xi$  is the main parameter determining the nature of fragmentation. For the purposes of this work,  $\xi = 11/6$  as will be explained more thoroughly below. By equation 2.7 above, the flux of fragmenting particles (particles that pass the  $m_f$  threshold) is given by coagulation:

$$F(m_f) \propto m_f^{v-2\alpha_c+3} \quad (2.10)$$

The fragmenting grains then turn into fragments that are redistributed to smaller masses. The backward flux of these particles is given by the conservation of mass, equation 2.5 above.

$$\frac{\partial F_f(m)}{\partial m} = -m n_f \quad (2.11)$$

So the flux of fragments to any mass,  $m$ , is given by integration of equation 2.11, from  $m_0$  to  $m$ :

$$\int_{m_0}^m -m n_f dm = \int_{m_0}^m N m^{1-\xi} dm \quad \rightarrow \quad F_f(m) \propto \frac{1}{2-\xi} (m^{2-\xi} - m_0^{2-\xi}) \quad (2.12)$$

The steady state is achieved by setting  $F_f(m_f) = -F(m_f)$  at the fragmentation mass. As mentioned above, for the purpose of this work,  $\xi = 11/6$ . This means that  $\xi < 2$  and thus  $m$  dominates  $F_f(m)$  above. Therefore, in the steady state the powerlaw parameters simplify to:

$$m^{v-2\alpha_c+3} \propto m^{2-\xi} \quad \rightarrow \quad \alpha_c = \frac{v + \xi + 1}{2} \quad (2.13)$$

The  $\xi$  used here represents a certain kind of fragmentation environment. It determines the shape of the flux of fragments, that is what mass of fragments that dominates. For example, cratering results mostly in small, low mass fragments while collisions between large, rigid grains can result in large, massive fragments.  $\xi$  is thus a complex parameter which takes into account the porosity and inner structure of the grains as well as collision types and grain size distribution. Observational and theoretical work has constrained  $\xi$  between 1 and 2 (Blum & Muench 1993) (Davis & Ryan 1990) (Ormel et al. 2009). Dohnanyi (1969) showed that coagulation/fragmentation steady states results in  $\xi = 1.83 \approx \frac{11}{6}$ . Mathis et al. (1977) and Draine & Lee (1984) showed that extinction and scattering in interstellar dust clouds can be simulated using  $\xi = 1.83 \approx \frac{11}{6}$ .

For this work, when  $m_f$  is reached the grains fragment and the resulting fragments should be evenly distributed among all masses up to  $m_f$ . This environment is secured by the condition  $\xi < 2$  for which  $m$  dominates equation 2.12. Fragments are redistributed to all  $m$ . A schematic picture of this can be seen in figure 2.1 below. The specific choice of  $\xi = 11/6$  is taken from Birnstiel et al. (2011) in order to make fitting functions to the theoretical grain size distribution. It is motivated by the works mentioned above.

The grains are assumed to grow sequentially, that is coagulation of similarly sized

grains dominates, see appendix A. This is thoroughly explained in section 3 of Makino et al. (1998).

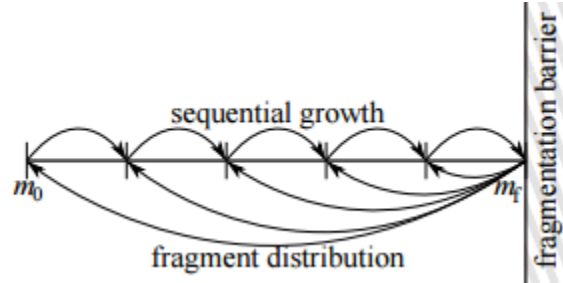


Figure 2.1: The  $\xi = 11/6$  environment for sequential dominated growth. At  $m_f$  the fragmentation velocity,  $u_f$ , is reached and the grains fragment. The flux of fragments is equally distributed, in mass, among all grain masses considered. This graph is taken from Birnstiel et al. (2011)

If, instead,  $\xi > 2$ ,  $m_0$  dominates and most of the fragments are redistributed to the monomer mass. This would result in the model described in section 2.1.1 (equation 2.7). Similarly if  $\xi < v - 2\gamma + 1$  fragments are mainly redistributed to large  $m$ . This can be seen in detail in Birnstiel et al. (2011). The mass distribution then becomes dominated by large  $m$  which means that, in turn, coagulation is also dominated by large  $m$ . This would alter the sequential growth assumed in this work.

The result is only valid for finite flux of mass, equation 2.6. This is achieved by  $v - 2\gamma + 1 < \xi$  as can be seen in more detail in Birnstiel et al. (2011) and Makino et al. (1998).

The resulting  $\alpha_c$  above, equation 2.13, is used in equation 2.3 to calculate the number distribution of the grain masses in the steady state. The parameter  $v$  of the collision kernel is central for the grain mass distribution. It depends on the relative velocities, cross sections and settling effects of the grains in the protoplanetary disk.

## 2.2 Size regions

### 2.2.1 Relative velocity regions

The collisions, determining the collision kernel, leading to the growth by coagulation are determined by the relative velocities of grains. In the case where the number density of particles,  $n(m)$ , is independent of position in the medium:  $C_{m_1 m_2} = \Delta u \cdot \sigma_{cross}$ .

$\Delta u$  is the relative velocity of the colliding particles and  $\sigma_{cross}$  is the cross section of the collision. This means that the parameters  $v$  and  $\gamma$  are strongly dependent on the relative velocity and cross sections of the particles in the medium.

The cross section of colliding particles is simply determined by their sizes. The relative velocity depends on the region of motion, which in turn also depends on the sizes of the colliding particles. For the protoplanetary disk there are three regions of motion that are important. These are:

- 1, Brownian motion of the smallest grains
- 2, Turbulent motion region I
- 3, Turbulent motion region II, affecting the larger grains.

Brownian motion is due to the random motion of the gas in the protoplanetary disk. The smallest particles have their velocities changed by collisions with fast-moving atoms and molecules.

The gas of the protoplanetary disk is turbulent and constantly creates new eddy currents of varying scale. Dust particles are affected by the drag force of these turbulent currents and therefore align themselves to the eddies. However, since the dust particles have larger inertia than the gas, this alignment takes a certain time. This time is called the friction time  $\tau_f$ . Considering dust particles in a gas, the mean free path of gas particles is much longer than the size of the dust particles,  $a \ll \lambda$  ( $\lambda$  is the mean free path of the gas particles). This is called the Epstein regime and it defines the drag force that each particle feels from the gas in the protoplanetary disk. The Epstein regime results in a friction time,

$$\tau_f = \frac{\rho_s a}{\rho_g c_s}, \quad (2.14)$$

$\rho_g$  is the gas density (Dullemond & Dominik 2004). Clearly,  $\tau_f$  is large for large grains and vice versa. The friction time and the direction of the eddies creates relative velocities between dust particles.

An important parameter of the eddies is the crossing time,  $t_{cross}$ , that is the time it takes for a particle to cross an eddy current. For a small particle with friction time much smaller than the eddy crossing times,  $\tau_f \ll t_{cross}$ , and smaller than the largest lifetime,  $t_L$ , of the eddies, all the eddies are called type I. This means that the dust particle has time to completely align its velocity to that of the eddy. The relative velocity between these particles is thus determined fully by the gas motion and the particle is coupled to the gas.

For a large particle with friction time larger than the eddy crossing time,  $\tau_f \gg t_{cross}$ , or larger than  $t_L$  of the eddies, all the eddies are type II. This means that the dust particle has its velocity only slightly perturbed by the eddies. Therefore large particles are decoupled from the gas. As can be seen in section 2.5 below, the solids in the disk generally have larger velocities than the gas due to the gas pressure gradient. This means that the relative

velocities of these particles increase.

The different relative velocities arising due to these eddy types are called turbulence regions I & II. The relative velocity between particles in these regions is highly dependent on the friction time  $\tau_f$ . The friction time and the largest eddy lifetime are used to define the Stokes number, a measure of a particle's dynamical behavior (Ormel & Cuzzi 2007).

$$St = \frac{\tau_f}{t_L} \quad (2.15)$$

By approximating  $t_L \approx t_{orb} = \frac{1}{\Omega_K}$ , Stokes number can be written as  $St = \Omega_K \tau_f$ . Hereby,  $St \ll 1$  means that the particle is coupled to the gas.  $St \gg 1$  means that the particle is decoupled from the gas. The border between the turbulence region I & II is not well defined since the transition is expected to be very smooth. It is, however, a reasonable assumption that the transition lies close to  $\tau_f \sim t_L$ . In the Epstein regime defined above, Stokes number can be approximated as (Birnstiel et al. 2011):

$$St \approx \frac{a \rho_s \pi}{2 \Sigma_g} \quad (2.16)$$

The very smallest grains of the protoplanetary disk have relative velocities governed by Brownian motion:

$$\Delta u_{BM} = \sqrt{\frac{8k_b T (m_1 + m_2)}{\pi m_1 m_2}} \quad (2.17)$$

Where  $T$  is the mid plane temperature of the disk and  $k_b$  is the Boltzmann constant. From equation 2.17 it is clear that small particles gain the largest relative velocities and thus grow more effectively by coagulation. As particles grow in mass, the coagulation rate is slowed down (Brauer et al. 2008).

The relative velocities of small sized grains due to turbulence is given by the Stokes number, (Ormel & Cuzzi 2007):

$$\Delta u_I \propto |St_1 - St_2| \quad (2.18)$$

And relative velocities of larger grains due to turbulent motions is similarly given by Ormel & Cuzzi (2007):

$$\Delta u_{II} \propto \sqrt{St_{max}} \quad (2.19)$$

Where  $St_{max}$  is the largest Stokes number of the two particles.

These regions of motion, combined with the cross sections, lead to different collision rates and thus different  $v$  for the collision kernel, equation 2.1. The derivation and a table of  $v$  in the relative velocity regions can be found in Birnstiel et al. (2011).

The  $\alpha_c$  parameters for these regions are calculated by equation 2.13.  $\alpha_c$  is only dependent on  $\xi$  and  $v$  and by holding  $\xi$  constant in this work, only variations in  $v$  are important. The situation is complicated by the collision kernel. For a large  $v$  parameter  $C_{m_1, m_2}$  becomes large, but at the same time  $n(m)$  becomes small. This means that there must be a certain value of  $v$  that is optimal for maximum number of collisions.

## 2.2.2 Settling effects

In this section, the vertical structure of the disk is taken into account. As a result of angular momentum and gravity, the gas of the disk is concentrated towards the midplane of the disk. The vertical structure of the gas is in a steady state due to the hydrostatic equilibrium which balances the forces of gravity, pressure and turbulence.

The situation for dust particles in the disk is slightly more complicated due to settling. Settling starts playing a role as grains grow larger by coagulation and decouple from the gas motion. As mentioned in section 2.2.1, the decoupling is closely related to  $\tau_f$  and thus  $St$ . Particles with  $St \ll 1$  are coupled to the gas while  $St \gg 1$  means decoupled particles. For the dust settling effect, the exact border between these two regions is estimated in Birnstiel et al. (2011) as  $St = \alpha_t$ . Particles that are decoupled from the gas motion,  $St > \alpha_t$ , does not feel the gas pressure gradient (described in section 2.5) and thus settle to the midplane of the disk more easily. A simple treatment of this follows below.

The scale height of dust,  $H_d$ , and gas,  $H_g$ , are related by the viscosity and Stokes number, (Youdin & Lithwick 2007):

$$\frac{H_d}{H_g} = \sqrt{\frac{\alpha_t}{St}}, \quad \text{for } St > \alpha_t \quad (2.20)$$

One can deduce from this that small grains, having a small  $St$ , have scale heights comparable to the gas scale height.

For grains with  $St < \alpha_t$  a more rigorous approach for settling is used, see (Fromang & Nelson 2009). This method is used and explained in section 2.5 below. However, the general trend of settling is still the same: large grains settle towards the mid plane.

Taking settling into account, the collision kernel is slightly modified (Birnstiel et al. 2011) and the resulting  $v$ -parameter is then different for grains of sizes on either side of:

$$a_{sett} = \frac{2\alpha_t \Sigma_g}{\pi \rho_s} \quad (2.21)$$

from equation 2.16 and  $St > \alpha_t$ . This can be seen in section 2.3 below. Any calculated index  $\alpha_c$  from here on applies to the vertically integrated number density, simply given by:

$$N(m) = \int_{-\infty}^{\infty} n(m, z) dz \quad (2.22)$$

where  $z = 0$  represents the midplane of the disk.

### 2.2.3 Grain size regimes

The result of the coagulation/fragmentation, settling and relative velocities of grains is that the vertically integrated number density,  $N(m)$ , of each grain mass can be calculated by a simple power law according to equation 2.3.  $N(m)$  is converted into a dust size distribution,  $N(a)$ , by equation 2.8. As described in the sections above,  $\alpha_c$  is determined by equation 2.13, which varies with grain size  $a$  due to the different size regions.

The size regions of interest are the following, as calculated by the preceding equations and Ormel & Cuzzi (2007):

The Brownian motion region upper limit:

$$a_{BT} \approx \left( \frac{8\Sigma_g}{\pi\rho_s} Re^{-1/4} \sqrt{\frac{\mu m_p}{3\pi\alpha_t}} \left( \frac{4\pi\rho_s}{3} \right)^{-1/2} \right)^{2/3} \quad (2.23)$$

As mentioned above, the transition region between the turbulence I & II is not well defined. For this work the transition grain size is given in Birnstiel et al. (2011) by:

$$a_{12} = \frac{2\Sigma_g}{y_a \pi \rho_s} Re^{-1/2} \quad (2.24)$$

Reynolds number  $Re \approx \frac{\alpha_t \Sigma_g \sigma_{H_2}}{2\mu m_p}$  with  $\sigma_{H_2}$  as the cross section of molecular hydrogen,  $\mu = 2.3$  as the mean molecular weight and  $m_p$  being the proton mass. The factor  $y_a \approx 1.6$  (Ormel & Cuzzi 2007).

The size above which settling effects apply to the grains is given by equation 2.21 above.

## 2.3 Simulations

The theory from previous sections is used to simulate grain size distributions in proto-planetary disks. In section 5 of Birnstiel et al. (2011) a recipe for a fitting function to the theoretical grain size distributions is provided. The recipe is used to obtain grain size distributions for this report. The program was thus created by me and later modified for further calculations of opacity etc.

Here, only the main features of the programming is described. For the full recipe of the grain growth simulations see Birnstiel et al. (2011).

### 2.3.1 Fragmentation and cratering

The theoretical models described does not take into account cratering. Particles colliding with  $\Delta u > u_f$  undergo fragmentation or cratering. Cratering is caused by small grains colliding with larger grains at high velocities. The small grains are not large enough to fragment the larger grains but instead carve out a small crater from the large grains. For the simulations, the size for when cratering becomes important is given by the relative velocity of monomers:

$$\Delta u^{mon} \geq u_f - \delta u \quad (2.25)$$

Where  $\delta u$  is the transition velocity between coagulation and fragmentation. There is no sharp distinction between these two regions. For the purposes of this report  $\delta u = 0.2$ . Fragmentation is instead caused by similarly sized grains colliding at great speed. The grain size for when fragmentation becomes important is therefore given by the relative velocity of equally sized grains:

$$\Delta u^{eq} \geq u_f - \delta u \quad (2.26)$$

At a certain grain size all of the colliding particles are assumed to fragment:

$$\Delta u^{eq} \geq u_f \quad (2.27)$$

In the simulations of the grain size distribution, both relative velocities of collisions with monomers,  $\Delta u^{mon}$ , and collisions with similarly sized grains,  $\Delta u^{eq}$  will be considered for the turbulence regions in order to simulate the fragmentation/cratering. These are given by the following fitting functions, see Birnstiel et al. (2011):

$$\Delta u^{mon} = u_{gas} \begin{cases} Re^{\frac{1}{4}}(St - St_0) & \text{for } a < a_{12} \\ (1 - \epsilon)Re^{\frac{1}{4}}(St - St_0) + \epsilon\sqrt{3St} & \text{for } a_{12} \leq a < 5a_{12} \\ \sqrt{3St} & \text{for } a \geq 5a_{12} \end{cases} \quad (2.28)$$

$$\Delta u^{eq} = \begin{cases} 0 & \text{for } a < a_{12} \\ \sqrt{\frac{2}{3}}\Delta u^{mon} & \text{for } a > a_{12} \end{cases} \quad (2.29)$$

$$u_{gas} = c_s \sqrt{\frac{3}{2}\alpha_t} \quad c_s = \sqrt{\frac{k_b T}{\mu m_p}} \quad \epsilon = \frac{a - a_{12}}{4a_{12}} \quad (2.30)$$

And thus the fragmentation and cratering can be related to certain grain sizes. Note that the redistribution of mass due to cratering is actually not included in the steady state theory. The behavior of  $N(a)$  due to cratering will thus only be simulated.

### 2.3.2 Grain size distribution

First, a logarithmic size grid is defined as  $a(j+1) = 1.12a(j)$  with the monomer size  $a(0) = a_0 = 0.025\mu m$ . The grain size regimes from equation 2.21, 2.23 and 2.24 and the upper size limits due to fragmentation and cratering, equations 2.25, 2.26 and 2.27, are implemented. The vertically integrated number distribution of grains is then simulated for each size by equation 2.3, 2.13 and 2.22:

$$N(m) \propto m^{-\alpha_c} \quad (2.31)$$

As mentioned above, the simulations made in this work are fitting functions to the real dust number density  $N(m)$ . This is easily translated into a size distribution by equation 2.8:

$$N(a) \propto a^{2-3\alpha_c}$$

For reasons that will become clear later, the grain size distribution is here expressed as  $N(a) m da$ , a function of the grain size  $a$ . The fitting function used to describe this  $N(a) m da$  is:

$$f(a) \propto a^\delta \quad (2.32)$$

where  $\delta$  is a parameter closely related to  $\alpha_c$ . A large  $\delta$  is equivalent to a small  $\alpha_c$ . It is given for the considered size regions in table 1 below (Birnstiel et al. 2011).

Regime	$\delta$	
	$a < a_{sett}$	$a > a_{sett}$
Brownian motion	3/2	5/4
Turbulence I	1/4	0
Turbulence II	1/2	1/4

Table 1:  $\delta$ -parameter for the grain size regimes.

The various values of  $\delta$  in the different size regions results in a size distribution of varying slope. The transition regions between the size regions are adjusted to make the distribution continuous. The resulting power-law distribution is shown in figure 2.2 along with the size regions of interest.

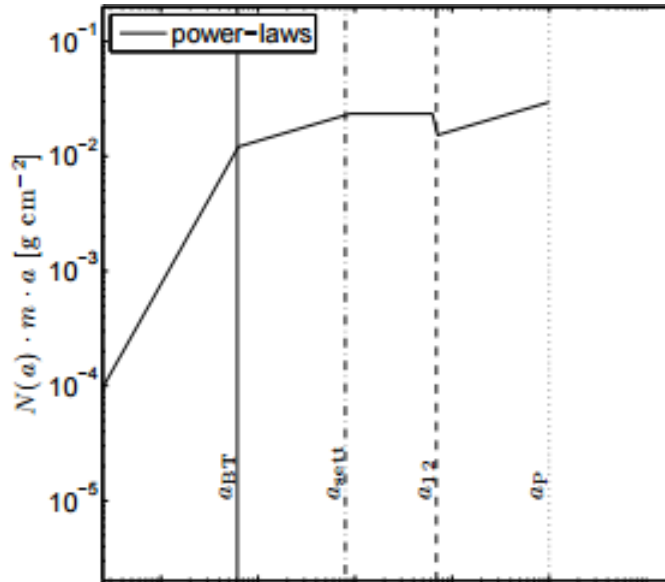


Figure 2.2: Power-law mass density distribution of dust sizes according to  $\delta$  and  $f(a) \propto a^\delta$ . The various size regions are included in the graph.  $a_P$  corresponds to the size where fragmentation becomes important, that is equation 2.26 of this report. The graph is taken from Birnstiel et al. (2011) and the parameters used are:  $\Sigma_g = 20 \text{gcm}^{-2}$ ,  $\alpha_t = 0.0001$ ,  $u_f = 100 \text{cm/s}$ ,  $\xi = 1.833$ ,  $T = 50 \text{K}$ ,  $\rho_s = 1.6$ . The number distribution has actually been normalized.

At the larger grain sizes, approaching fragmentation and cratering sizes, the steady state size distribution features a bump. This bump is due to the assumption that similarly

sized grain growth dominates the coagulation. A grain of certain size preferably collides and coagulates with an arbitrary set of neighboring sizes, both bigger and smaller grains. At large grain sizes the grains have fewer upper sizes to combine with, due to the maximum size,  $m_f$ . In order to keep the flux of mass constant (equation 2.5) even at these sizes there must be more large grains to compensate for the lack of grains above  $m_f$ . Cratering amplifies this effect by constantly eroding the large grains, thus making them grow at slower rates. The over-density of large grains is simulated by help of the upper size limits, equations 2.25, 2.26 and 2.27.

The fitting function,  $f(a)$ , is then normalized with  $\Sigma_d$ , as calculated by the assumed metallicity  $Z \approx \frac{\Sigma_d}{\Sigma_g}$ , as well as the sum of the fitting functions for each grain size. This results in the number density of grain sizes,  $N(a) m da$  (vertically integrated).

$$N(a) m da = \frac{f(a)\Sigma_d}{\sum f(a)} \quad (2.33)$$

An integration of the size number density over all sizes returns the dust surface density:

$$\int_{a_0}^{a_{max}} N(a) m da = \Sigma_d \quad (2.34)$$

The disk model (Bitsch et al. 2015) described in the introduction, can now be applied to the simulations to get all the needed physical parameters to calculate  $N(a) m da$  at all disk radii  $R$ . This can be done for various epochs of the protoplanetary disk and the result is shown in figure 3.1 in the result section. The parameters that are given by the disk model are:  $T$ ,  $\Sigma_g$ ,  $R$  and  $H_g$ . Most of the other input parameters can be set to constants, such as  $\rho_s$ ,  $\mu$  etc. However, there are four more important parameters that crucially determine the results. These are:

The turbulence strength,  $\alpha_t$ , the metallicity,  $Z$ , the fragmentation velocity,  $u_f$ , and the time epoch  $t$  (defines  $\dot{M}$  of the disk and thus affects all of the disk parameters).

These parameters have well defined, small ranges of values and thus the grain size number density,  $N(a) m da$ , has to be evaluated within these.

Clearly, the fragmentation velocity  $u_f$  affects the maximum grain size of the distribution. This is because of the increased relative velocities of larger grains. By allowing larger relative velocities, larger grains can exist.

The metallicity directly affects the dust surface density  $\Sigma_d$  and thus scales up or down the distribution accordingly through the normalization (equation 2.33).

The turbulence strength  $\alpha_t$  affects the the relative velocity of all particles due to  $u_{gas}$  in equation 2.30 and Reynolds number,  $Re$ . Thus the relative velocity regions and the fragmentation barrier  $m_f$  are all heavily dependent on  $\alpha_t$ . The turbulent strength also affects the settling. Larger turbulence leads to less settling and this moves  $a_{sett}$  to larger grain sizes (equation 2.21).

The time epoch defines  $\dot{M}$  and thus affects all the important parameters from the disk model  $\Sigma_g$ ,  $H_g$  and  $T$ . Generally, all three parameters decreases with time.

## 2.4 Opacity

A well defined number density of grains,  $N(a) m da$ , of different sizes has now been obtained at all radii,  $R$ , of the protoplanetary disk model. The grain size distribution program is modified to calculate the opacity of the protoplanetary disk model.

The program RADMC 3D by C. P. Dullemond is used to calculate opacity,  $\kappa_i(T)$ , for various sizes of grains at a range of temperature, assuming a certain dust density.<sup>1</sup> The opacity was calculated in a range of temperature for 18 different grain sizes, varying from  $a^{OP}(1) = 0.025\mu m$  to  $a^{OP}(18) = 100mm$ . The porosity and composition of the grains are set to be the same as in the disk simulations (Bitsch et al. 2015).

The  $\kappa - T$  relation for each of the new grain sizes can be seen in figure 2.3.

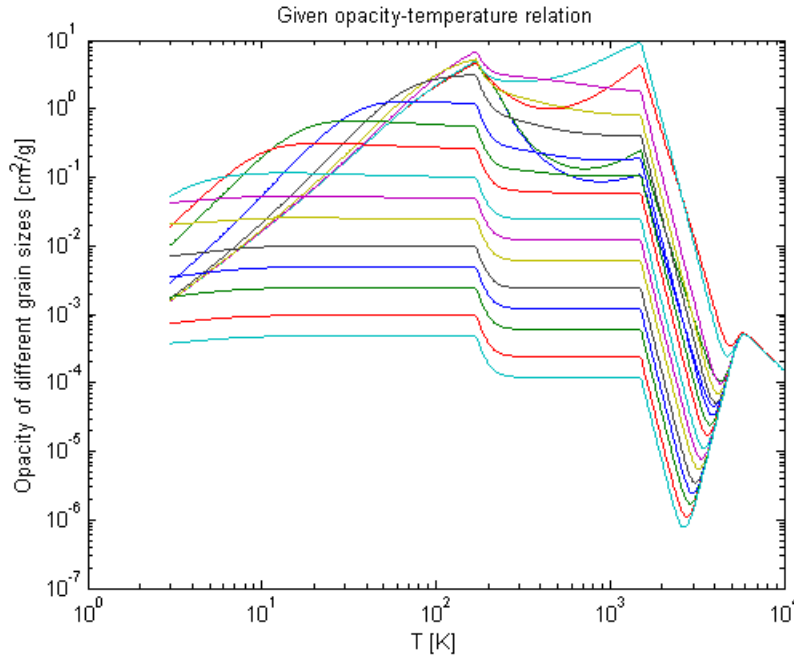


Figure 2.3: Opacity as a function of temperature for the 18 different grain sizes,  $a^{OP}$ , as calculated by RADMC 3D.

The size bins used for the opacity are thus larger and fewer than the bins of the

<sup>1</sup><http://www.ita.uni-heidelberg.de/~dullemond/software/radmc-3d/>

logarithmic grain size grid defined in section 2.3 above. The width of the new size bins is defined as:

$$\Delta a^{OP}(i) = \left( a^{OP}(i) - \frac{a^{OP}(i) - a^{OP}(i-1)}{2} \right) - \left( a^{OP}(i) + \frac{a^{OP}(i+1) - a^{OP}(i)}{2} \right) \quad (2.35)$$

Each  $a^{OP}(i)$  thus incorporates a number of sizes  $a(j)$  from the logarithmic size grid defined in section 2.3. Each of these sizes  $a(j)$  are accompanied by a number density,  $N(a) m da$ , for each orbital distance,  $R$ , of the protoplanetary disk.  $i$  is the index of the 18 new sizes.

The dust surface density,  $\Sigma_d(i)$ , of each of the new size bins is then simply the summation of the number densities of all the former size bins,  $a(j)$ , that lies within the borders of  $\Delta a^{OP}(i)$ . This can be clearly understood by equation 2.34.

$$\Sigma_d(i) = \sum_j N(a_j) m da_i \quad (2.36)$$

Where  $a(j)$  lies within the interval  $\Delta a^{OP}(i)$ .

$\Sigma_d(i)$  of each of the new grain size bins is important for weighing the influence of each opacity bin  $\kappa_i(T)$ . In this way, a mean opacity of the disk due to the dust size distribution can be calculated.

### 2.4.1 Midplane density

The program used to calculate opacity of each grain size is only dependent on  $T$ . For the disk simulations used, only the mid plane temperature is given. The surface density of all grain sizes,  $\Sigma_d(i)$ , in the disk model thus has to be translated into a midplane dust density,  $\rho_{d,0}(i)$ . The same transformation is also made for the gas surface density,  $\Sigma_g$  into  $\rho_{g,0}$ .

In order to calculate  $\rho_{g,0}$  the same approach is used as in Dullemond (2013). The vertical temperature distribution is assumed to be uniform for simplicity,  $\frac{dT}{dz} = 0$ . The speed of sound in the disk is given by:  $c_s = \sqrt{\frac{k_b T}{\mu m_p}}$ , which means that  $\frac{dc_s^2}{dz} = 0$ .

The vertical structure of the gas in the disk is in an equilibrium between pressure and gravity and thus hydrostatic equilibrium gives:

$$\frac{dP}{dz} = -\rho \frac{GM_{star}}{R^3} z \quad (2.37)$$

But the keplerian rotational frequency  $\Omega_K$  can be expressed as:

$$\Omega_K = \sqrt{\frac{GM_{star}}{R^3}} \quad \text{or} \quad \Omega_K = \frac{c_s}{H} \quad (2.38)$$

And the pressure of the disk as:

$$P = \rho c_s^2 \quad (2.39)$$

Remembering the vertical approximation made for  $c_s^2$  above, the hydrostatic equilibrium simplifies to:

$$\frac{1}{\rho} \frac{d\rho}{dz} = -\frac{\Omega_K^2}{c_s^2} = -\frac{1}{H^2} \quad (2.40)$$

The solution to this is:

$$\rho(z) = \rho_0 e\left(-\frac{z^2}{2H^2}\right) \quad (2.41)$$

Where  $\rho_0$  is the midplane density. This is a gaussian density distribution. The surface density can be then expressed as the integration of the density over all heights above mid plane,  $z$ , similar to equation 2.22. This is used to replace  $\rho$  in the equation above, with the known  $\Sigma$  to solve for  $\rho_0$ .

$$\Sigma = \int_{-\infty}^{\infty} \rho dz \quad (2.42)$$

$$\rho_0 = \frac{\Sigma}{\int_{-\infty}^{\infty} e\left(-\frac{z^2}{2H^2}\right) dz} \quad (2.43)$$

The integral in the demominator can be solved analytically to obtain the final expression for the midplane density:

$$\rho_0 = \frac{\Sigma}{\sqrt{2\pi}H} \quad (2.44)$$

Equation 2.44 can easily be used to calculate the midplane gas density since the disk model used provides both  $H_g$  and  $\Sigma_g$ . By approximating the vertical structure of the dust to be similar to that of the gas this method could in theory be applied to the dust as well. However, although  $\Sigma_d(i)$  has also been obtained above, there is no simple way of calculating the scale ratio  $H_d$  for the dust at all grain sizes (equation 2.20 only applies when  $St > \alpha_t$ ).

In order to calculate the midplane dust density, the approach of Fromang & Nelson (2009) is adopted. This approach describes the vertical equilibrium state of the dust by including transport of dust particles by turbulence. Considering the turbulence as diffusion leads to a new equation describing the equilibrium between diffusion and settling of the dust. The complete method will not be described in detail here but can instead be found in section 3.2.1 of Fromang & Nelson (2009).

$$\rho_d(i) = \rho_{d,0}(i) \exp \left[ -\frac{[\Omega_K \tau_f(i)]_{mid}}{\alpha_t} \left( e^{\left(\frac{z^2}{2H^2}\right)-1} - \frac{z^2}{2H^2} \right) \right] \quad (2.45)$$

Here,  $\tau_f(i)$  is the friction time of the grain sizes  $a^{OP}(i)$ . It is given by Dullemond & Dominik (2004):

$$\tau_{f,mid}(i) = \frac{\rho_s a^{OP}(i)}{\rho_{g,0} c_s} \quad (2.46)$$

The same method as for the midplane gas density is used, substituting equation 2.42 into 2.45 above results in:

$$\rho_{d,0}(i) = \frac{\Sigma_d(i)}{int} \quad (2.47)$$

Where  $int$  is the integral of equation 2.45 above with respect to  $z$  (from  $-\infty$  to  $\infty$ ). This has to be solved numerically.  $\rho_{d,0}(i)$  is then evaluated separately for all grain sizes  $a^{OP}(i)$ .

## 2.4.2 Weighted mean opacity

The weighted mean opacity is calculated using the midplane dust density for each grain size  $a^{OP}(i)$  as obtained above by equation 2.47, for each of the 18 grain sizes, and their calculated opacities  $\kappa_i(T)$ .

$$\bar{\kappa}(T) = \sum \frac{\rho_{d,0}(i)\kappa_i(T)}{\sum \rho_{d,0}(i)} \quad (2.48)$$

This can be repeated for all of the evolutionary stages of the protoplanetary disk (different parameters  $T$ ,  $\Sigma_g$ ,  $R$  and  $H_g$ ). The resulting opacity-orbital distance function is then plotted and shown in the result section, see figure 3.4.

## 2.5 Radial drift

As stated above, the coagulation/fragmentation model used to calculate the grain size distribution only considers fragmentation as the upper size limit. However, there is another important process for the upper size limit, which has been omitted in this work, namely the radial drift. This section justifies the approach.

The material of the protoplanetary disk is mainly in gas form. The gas of the disk therefore experiences pressure in a way that the much more scarce solid particles do not. The gas is in hydrostatic equilibrium, both vertically and horizontally, which means that there will be a pressure gradient to counteract gravity. Horizontally, that means larger gas pressure towards smaller orbital distances,  $R$ . At the same time, the rotation of the system causes a centrifugal force that contributes to the outward force on the gas. The sum of the pressure gradient force and the centrifugal force must cancel the gravitational force for an equilibrium state. Therefore, because of the pressure gradient, the gas has a smaller centrifugal force and thus less rotational velocity than dust. The gas of the protoplanetary disk rotates at sub-keplerian velocity.

Small dust particles ( $\tau_f/t_{orb} \ll 1$ , where  $t_{orb}$  is the orbital period of the grain) are coupled to the gas motion and thus also moves at sub-keplerian velocities. Larger particles are not coupled to the gas ( $\tau_f/t_{orb} \gg 1$ ) and do not feel the pressure gradient (Weidenschilling 1977). Therefore they should move at keplerian rotational velocity. However, in reality the dust particles experience a constant drag force from the slower moving gas, comparable to that of moving in a headwind (Epstein regime). This means that the dust particles transfer angular momentum to the gas and drift inwards towards smaller  $R$ . At a certain distance from the central star, the grains evaporate. As particles grow by coagulation they gain increased cross sections which leads to larger drag force and thus quicker radial drift. For large particles, this drift velocity can be quite substantial. However, as the particles grow they also gain increased friction time,  $\tau_f$ , and more slowly lose velocity due to the drag force. This means that a certain, intermediate, particle size gains the largest radial drift. It is reasoned, in Weidenschilling (1977) that the lifetime of particles due to radial drift varies heavily due to the particle size. Particles in the size range  $a \sim 0.1 - 10^4 \text{ cm}$  has characteristic lifetimes well below the age of a typical protoplanetary disk (see figure 6 in

the Weideschilling paper). The shortest lifetimes achievable are on the order of  $\sim 100$  yrs.

The coagulation of dust particles is due to collisions. As the density of dust in the disk is relatively low, the mean collision time can be long, even comparable to the timescale of the radial drift. If the mean radial drift timescale is shorter than the mean growth timescale, this provides an obstacle for further growth. That means that the particles evaporate before reaching the fragmentation velocity. In Birnstiel et al. (2015) the upper size limits are expressed mathematically as:

$$a_{frag} = \frac{2}{3\pi} \frac{\Sigma_g}{\rho_s \alpha_t} \frac{u_f^2}{c_s^2} \quad (2.49)$$

$$a_{drift} = \frac{2}{\pi} \frac{\Sigma_d}{\rho_s |\gamma|} \frac{V_K^2}{c_s^2} \quad (2.50)$$

Here,  $V_K = \sqrt{\frac{GM_{star}}{R}} = \frac{\Omega_k}{R}$  is the keplerian velocity,  $\gamma = \frac{\partial \ln P}{\partial \ln R}$  is the pressure gradient and  $P = \rho c_s^2$  is the pressure of the gas in the disk.

Clearly, the smallest of these size thresholds is the dominating. The general trend in protoplanetary disk simulations, see Birnstiel et al. (2015), is that  $a_{frag}$  dominates at smaller  $R$  while  $a_{drift}$  takes over and dominates further out. The region where fragmentation dominates will be slightly top heavy. This means that grains of large sizes dominates the total mass distribution. It is simply a consequence of the grain size distribution due to coagulation/fragmentation presented above. In the region where radial drift dominates the total mass distribution will be even more top heavy. This is because without fragmentation there is no resupply of smaller sized grains. The larger grains simply just transition inwards in the system toward smaller  $R$ .

The thresholds are calculated by the model used above for all the orbital distances,  $R$ , considered in the disk model. Only the midplane is considered in the calculations. As can be seen in figure 2.4,  $a_{frag}$  is significantly smaller than  $a_{drift}$  for all  $R$ , even considering  $u_f = 1000$  cm/s. Therefore particles will most likely fragment before reaching the central star. This is the motivation to the simplification of considering only fragmentation.

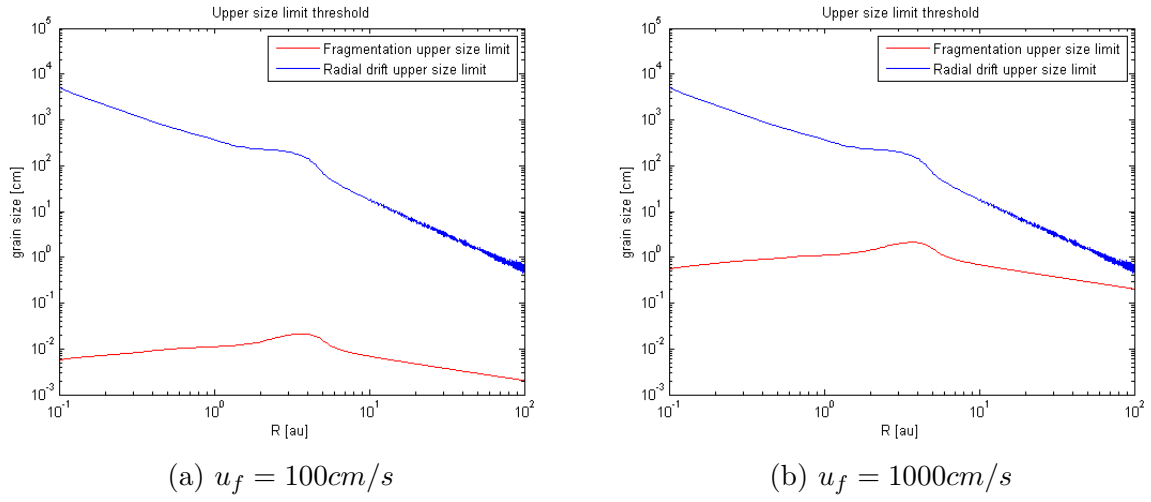


Figure 2.4: The 1 Myr upper size barriers due to fragmentation and radial drift for  $u_f = 100 \text{ cm/s}$ ,  $u_f = 1000 \text{ cm/s}$ ,  $Z = 0.5\%$  and  $\alpha_t = 0.0054$ .

# Chapter 3

## Results

The result section of this work is split into two parts. The first part covers the grain size distribution of the protoplanetary disk structure. How do the four variable parameters  $\alpha_t$ ,  $Z$ ,  $u_f$  and  $t$  affect the distribution? The second part evaluates the resulting weighted mean opacity of the disk profile. The impact of the four variable parameters is analyzed and the weighted mean opacity is compared to the Bell & Lin (1994) opacity from the all  $\mu m$  grain size disk in Bitsch et al. (2015).

All of the figures in this section are results of the simulations made in the program described and created in section 2.3 above.

### 3.1 Grain size distribution

First off, the grain size distribution,  $N(a) m da$ , at an orbital distance of  $R \sim 10au$  is displayed in figure 3.1. At that distance  $\Sigma_g$ ,  $H/R$  and  $T$  is given by the Bitsch et al. (2015) disk structure. In the disk simulations  $\alpha_t = 0.0054$  was used. The fragmentation velocity and the metallicity are  $u_f = 100cm/s$  and  $Z = 0.5\%$  which is within the estimated parameter ranges. For reference, these values are called the standard values.

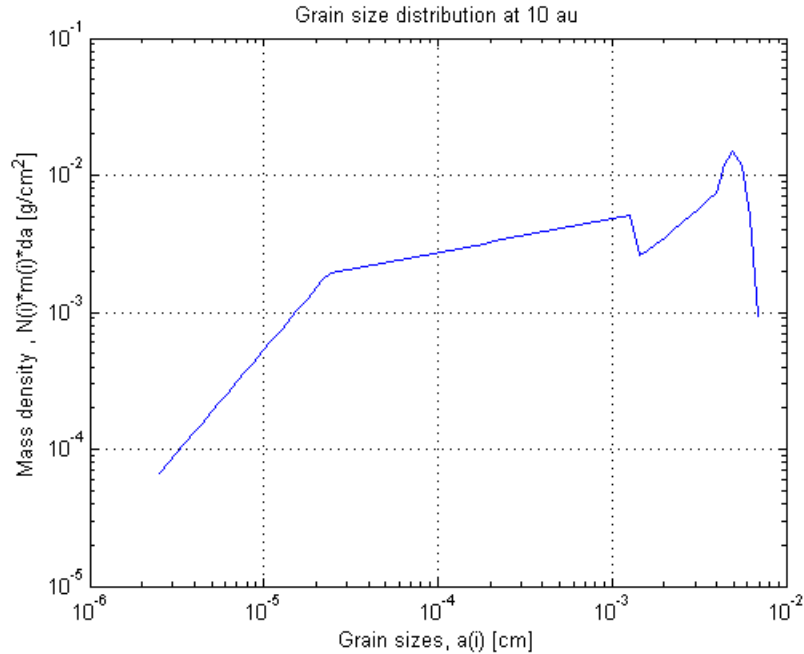


Figure 3.1: Dust size distribution at  $R \approx 10.02au$  for a 1 Myr old disk. The standard values for reference are  $u_f = 100cm/s$ ,  $Z = 0.5\%$ ,  $\alpha_t = 0.0054$ . ( $\Sigma_g \approx 43.59g/cm^2$ ,  $H/R \approx 0.042$ ,  $T \approx 43.13K$ )

The parameters displayed in the figure are the variables. The following parameters are the same for all the simulations:  $\rho_s = 1.6g/cm^3$ ,  $\mu = 2.3$  and  $\delta u = 0.2u_f$

The general features of the distribution are quite simple. The distribution is slightly top heavy, that is  $N(a) m da$  is dominated by large grains. This is intuitively expected because of the constant mass flux described in equation 2.5, meaning that all sizes coagulate at the same rate (in mass). Monomer size grains are only replenished by the flux of fragments which is equal for all considered sizes. Larger grains are replenished by both coagulation of smaller grains and the flux of fragments. The number of small grains is thus depleted in the steady state and the slope of the distribution,  $\delta$ , is generally positive.

The steep slope of the Brownian motion region, small  $a$ , is expected due to equation 2.17. At large  $m_1$  and  $m_2$ , the relative velocities due to Brownian motion is smaller than for small  $m_1$  and  $m_2$ . This means that growth by coagulation is the most effective at small particle masses, according to the collision kernel (Brauer et al. 2008). This results in a pile-up of larger grains in the steady state.

The more flat part that follows is due to the turbulence I region. The grains in this region are fully coupled to the gas motion and thus the relative velocities are not as

dependent on the grain sizes (see equation 2.18). Therefore,  $\delta$  is smaller and the resulting grain size distribution varies more slowly with increasing grain size  $a$ .

The transition between turbulence I and II is the gap at roughly  $a \sim 10^{-3}$ . The gap is caused by the sudden change in relative velocities from particles with  $\tau_f$  small enough to be completely aligned to the turbulent gas motion, to particles with  $\tau_f$  large enough to only be perturbed by the turbulence eddies. Due to equation 2.19 the decoupled gas particles are increasingly less affected by the gas motion as their sizes increase. This means that their relative velocities increase with particle size. Growth by coagulation thus increase with  $a$  in this region. This causes depletion of the particles on the  $a_{12}$  border in the steady state. The slope of the turbulence II region is positive due to the top heavy distribution and the pile-up effect at the largest grain sizes.

The final region is the cutoff at large  $a$ , with large number densities of grains. This is, as explained in section 2.3, because of the pile-up of large grains due to lack of larger companions and erosion by cratering.

The settling of grains above  $a_{sett}$  provides another transition somewhere in the grain size distribution. The location of this transition is heavily dependent on  $\alpha_t$  as can be seen in equation 2.21. For sufficiently large values of  $\alpha_t$ , the settling region will not be visible within the range of sizes presented here, as is the case for figure 3.1. Particles that are large enough to settle into the midplane will have increased collision probabilities. This means that, in order to preserve the constant mass flux the grains at these sizes has to be fewer.  $\delta$  is therefore decreased at  $St > \alpha_t$  and the slope is more flat as a result.

In the protoplanetary disk profiles given by Bitsch et al. (2015) the input parameters ( $\Sigma$ ,  $H$  and  $T$ ) vary with orbital distance  $R$ . The resulting grain size distribution has different shapes for each  $R$ . Furthermore, the parameters  $u_f$ ,  $\alpha_t$ ,  $Z$  and  $t$  can be varied each simulation for more variety in the resulting distributions. The general effects of these changes are described below.

The fragmentation velocity  $u_f$  has great impact on the grain size distribution. It enters through the upper grain sizes described in the fragmentation/cratering section (see equation 2.27). Clearly, a greater  $u_f$  results in a greater maximum relative velocity  $\Delta u_{II}$ .  $\Delta u_{II}$  is directly linked to the square root of the grain size  $a$  through equation 2.19. Therefore, the largest grain size is related to the fragmentation velocity as:

$$a_{max} \propto u_f^2 \quad (3.1)$$

According to equations 2.19 and 2.27 the  $\Delta u_{II}$  region grows with  $u_f$ . This trend can also be seen in figure 3.2. In order to preserve the total  $\Sigma_d$  in the disk the size distribution of the smaller grains must decrease with increasing  $u_f$ . This is secured by the normalization in equation 2.33.

The effects of changing the viscosity parameter,  $\alpha_t$ , are quite numerous. The most profound effects are described here. First of all, increased  $\alpha_t$  leads to increased turbulence in the protoplanetary disk. Thus all relative velocities are slightly increased and the whole size distribution,  $N(a) m da$ , is shifted to smaller grain sizes  $a$ . To preserve the total  $\Sigma_d$  in the disk the number distribution of all grain sizes must then increase (equation 2.33). The dependence of the relative velocities on  $\alpha_t$  can be seen in equation 2.30.

For increasing  $\alpha_t$  the region where settling starts becoming important moves to larger sizes while all the relative velocity regions moves to smaller sizes (see equations 2.21, 2.23 and 2.24). The  $\alpha_t = 0.0054$  used in Bitsch et al. (2015) for the disk structure, and thus the most commonly used  $\alpha_t$  used in this work, is quite large. This means that the settling region has moved to very large grain sizes. At many places of the disk, and for many epochs this means that settling doesn't occur at all. The lack of the transition region due to settling can be noticed for large  $\alpha_t$  in figure 3.2.

By varying the metallicity,  $Z$ , the dust surface density,  $\Sigma_d$ , relative to  $\Sigma_g$  is changed. Increasing  $\Sigma_d$  means increased total mass in the system and thus increased number of particles. In the simulations this comes from the normalization of  $f(a)$  with  $\Sigma_d$  (equation 2.33). The metallicity thus varies only the total  $N(a) m da$  of all sizes  $a$  in the distribution. The size regimes remain unchanged.

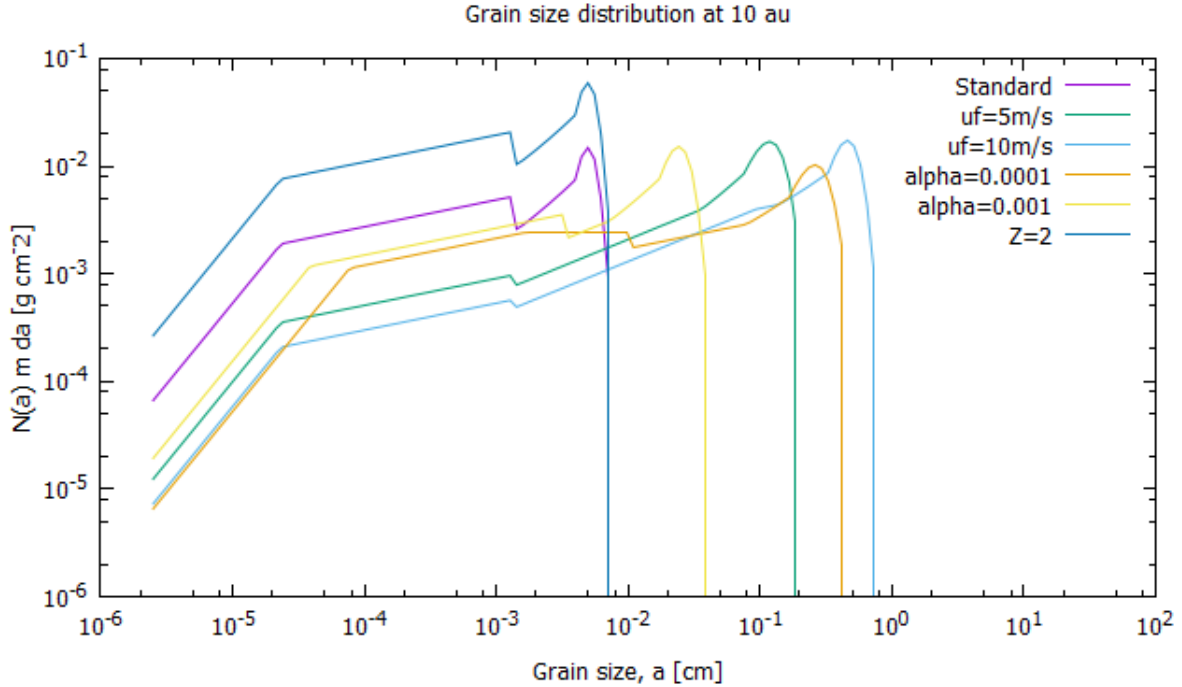


Figure 3.2: The resulting grain size distributions for various grain sizes at an arbitrary orbital distance of  $R \approx 10.02au$ . The parameters  $u_f$ ,  $Z$  and  $\alpha_t$  are changed one by one from the standard parameters in figure 3.1 as reference. All the dust distributions above are from the 1 Myr epoch. ( $\Sigma_g \approx 43.59g/cm^2$ ,  $H/R \approx 0.042$ ,  $T \approx 43.13K$ )

The gas surface density  $\Sigma_g$ , the temperature  $T$  and the gas scale height  $H_g$  are all central in the grain size distribution simulations. The structure of  $\Sigma_g$ ,  $T$  and  $H_g$  can be seen in figure 1.1 in the introduction.

The gas surface density  $\Sigma_g$  enters through the relative velocity regions (equations 2.21, 2.23 and 2.24). Furthermore equation 2.16 shows that  $\Sigma_g$  is inversely proportional to  $St$ . Clearly, increased  $\Sigma_g$  leads to decreased relative velocities and thus  $a_{BT}$  and  $a_{12}$  move to larger grain sizes,  $a$ . Decreased  $St$  results in increased fragmentation size  $a_{max}$  due to equations 2.19 and 2.27. Equation 2.21 shows that the settling barrier also increases with  $\Sigma_g$ . Furthermore, the dust surface density  $\Sigma_d$  is highly dependent on  $\Sigma_g$  through the metallicity,  $Z$ . All of the effects described means that increased  $\Sigma_g$  leads to both larger  $N(a) m da$  at all  $R$  and a shift towards larger sizes,  $a$ .

The midplane temperature  $T$  affects the relative velocities between particles through equation 2.30. Large  $T$  leads to large  $\Delta u$  which reduces the fragmentation barrier  $a_{max}$ . However,  $T$  does not affect the size regions  $a_{BT}$ ,  $a_{sett}$  and  $a_{12}$  which means that the influence of the turbulence II region is heavily affected. The total  $\Sigma_d$  remains unaffected.

The scale height,  $H_g$ , is related to both the midplane density,  $\rho_0$ , through equations 2.44 and 2.47, and the temperature,  $T \propto \left(\frac{H}{R}\right)^2$ . It affects the dust size distribution accordingly through  $\Sigma_g$  and  $T$ .

The grain size distribution is simulated over all  $R$  considered in the disk model. The result is a grain size distributions similar to the ones displayed above with differences according to the parameter changes  $\Sigma_g$ ,  $T$  and  $H_g$  described above. An interesting result is to plot the size distribution over the whole disk as in figure 3.3 below. This is done for the 0 Myr, 1 Myr and 2 Myr epochs. The colour of the plot represents the number distribution,  $N(a) m da$ , of each grain size at a certain orbital distance  $R$ .

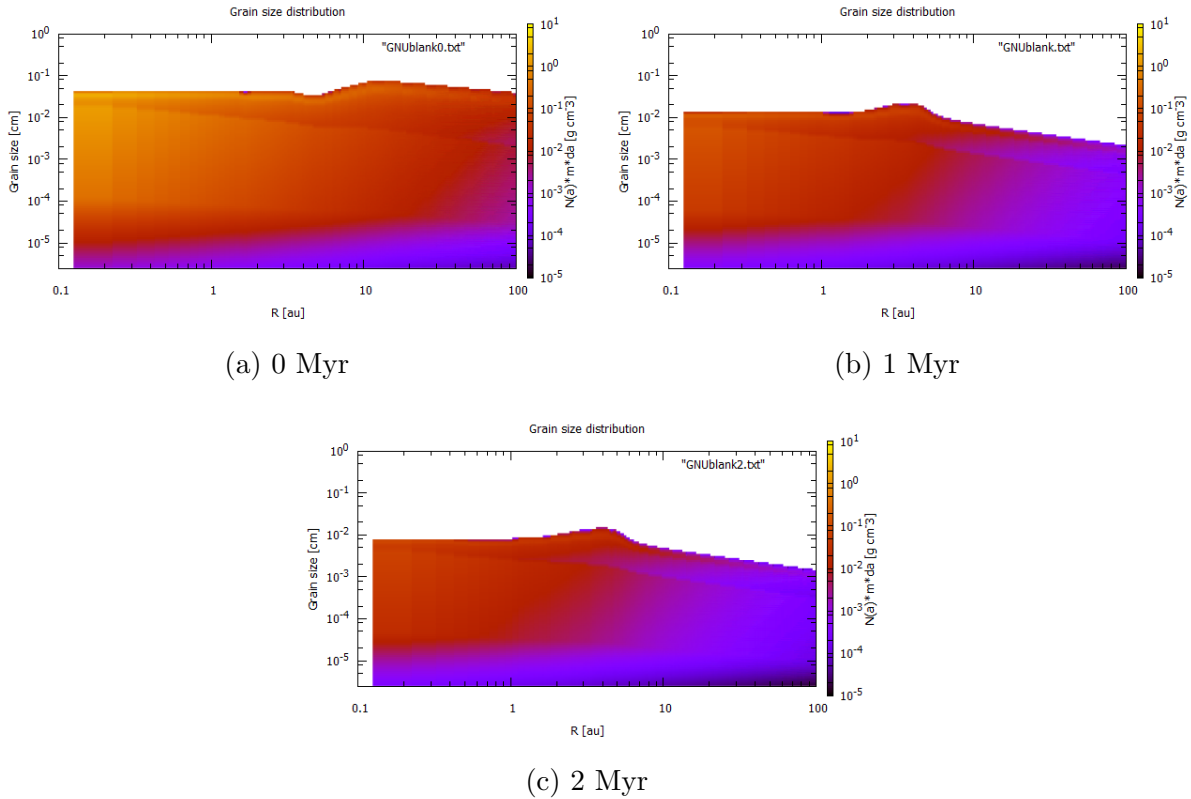


Figure 3.3: Grain size distribution over the whole disk structure (all  $R$ ). All the simulations were made with  $u_f = 100\text{cm/s}$ ,  $Z = 0.5\%$  and  $\alpha_t = 0.0054$  for three different epochs.

Clearly, there is more dust in the disk (large  $\Sigma_d$ ) at early epochs than at later stages, as expected. Larger grain sizes are also available at early stages. At later epochs the larger grains are not reachable, mainly because of decreased  $\Sigma_g$  and  $\Sigma_d$ .

## 3.2 Opacity

The mean weighted opacity described in equation 2.48 is highly dependent on the surface density of each grain size, which is calculated from the grain size distribution. If a certain grain size has a large  $\Sigma_d$  its opacity has a distinct contribution to the weighted mean opacity. From the grain size distributions simulated, see figures 3.1, 3.2 and 3.3, it is evident that larger grains have greater  $\Sigma_d$  than the smaller sizes. The size distribution is top-heavy and large grains dominate the opacity. The weighted mean opacity for a set of various parameters is displayed below, figure 3.4.

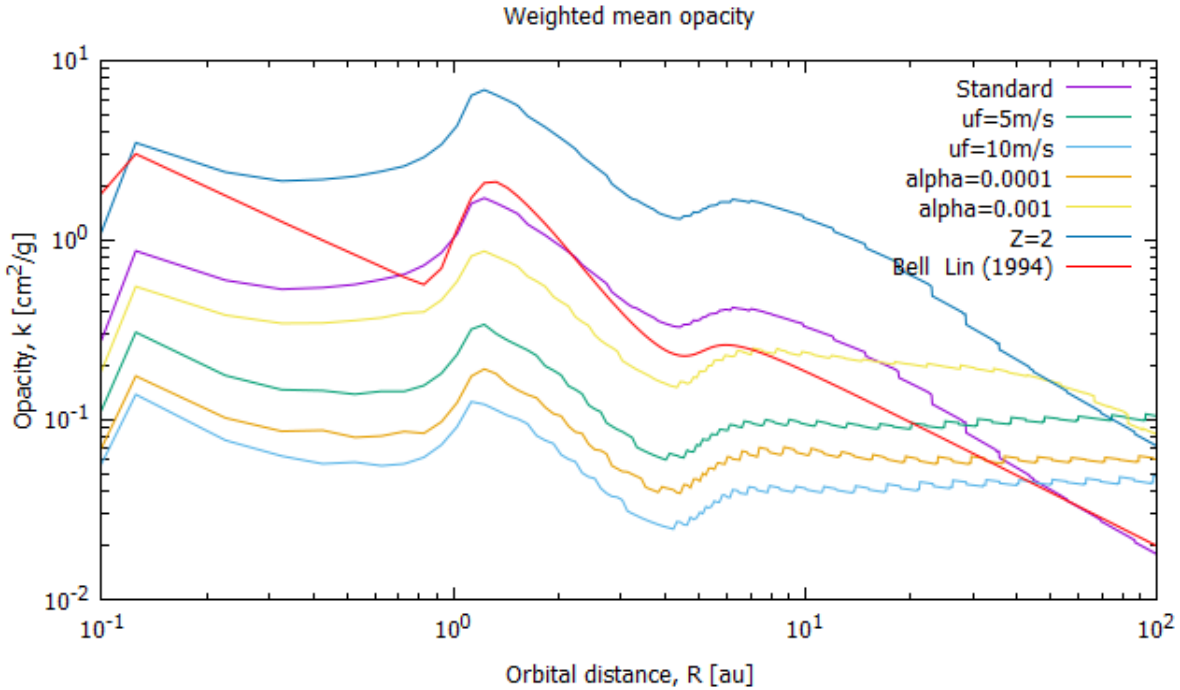


Figure 3.4: Weighted mean opacity as function of orbital distance considering all grain sizes. The weighted mean opacity from equation 2.48 is compared with the Bell & Lin (1994) opacity of the Bitsch et al. (2015) disks with only  $\mu m$  sized dust (red line in the figure). The figures above are all from the 1 Myr epoch. The parameters  $u_f$ ,  $Z$  and  $\alpha_t$  are changed one by one from the standard parameters in figure 3.1 as reference. The weighted mean opacity above is from the 1 Myr epoch with input parameters from the whole disk (Bitsch et al. 2015) (all orbital distances).

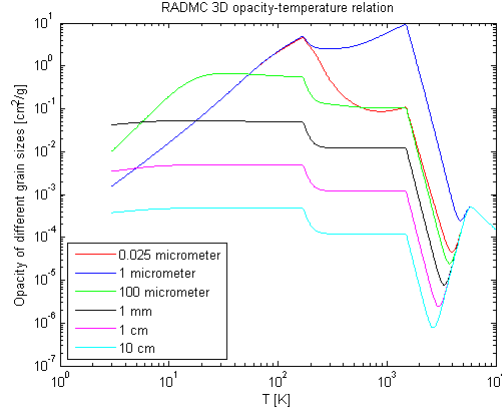


Figure 3.5: Opacity as a function of temperature for a few of the considered grain sizes, as calculated by RADMC 3D.

The changes in the weighted opacity due to the parameters  $\alpha_t$ ,  $u_f$  and  $Z$  are closely related to the changes in the dust size distributions as described in section 3.1. The general trend of figure 3.5 is that larger grains have lower opacity. A parameter change that leads to large sizes dominating the dust distribution thus leads to an overall decrease in opacity. For example, increasing  $u_f$  allows for bigger dust grains in the size distribution. The total  $\Sigma_d$  is preserved and the distribution becomes more top-heavy which in turn results in overall less mean opacity (see figure 3.5).

Similarly,  $\alpha_t$  shifts the size distribution,  $N(a) m da$ , in size,  $a$ . The total  $\Sigma_d$  is not changed. Increased  $\alpha_t$  causes increased  $\Delta u$  and therefore smaller  $a_{max}$ . The number of grains is increased to preserve  $\Sigma_d$  and the opacity increases accordingly.

$Z$  affects only the total  $\Sigma_d$  of the disk. More grains simply give rise to greater opacity.

The changes in opacity due to  $T$ ,  $\Sigma_g$  and  $H_g$  are straightforward, considering the changes in  $N(a) m da$  in section 3.1.

# Chapter 4

## Conclusions

As can be seen in figure 3.4 for the 1 Myr disk structure, the mean opacity varies quite a bit with the considered parameter spaces in  $u_f$ ,  $Z$  and  $\alpha_t$ . Some certain parameters allows for a mean opacity that closely resembles the Bell & Lin (1994) opacity of only  $\mu m$  sized grains that was used in the disk simulations (see figure 3.4(a)). For  $u_f = 100 cm/s$ ,  $Z = 0.5\%$  and  $\alpha_t$  in the 1 Myr disk the approximation made by Bitsch et al. (2015) is good. However, for other sets of the parameters described above the mean opacity can vary from the Bell & Lin (1994) opacity by several orders of magnitude. In these cases the approximation is clearly not a good one. The validity of the only  $\mu m$  sized grains depends highly on which values of  $u_f$ ,  $Z$  and  $\alpha_t$  are the correct ones.

The fragmentation velocity,  $u_f$ , of the model is dependent on the exact dust composition. The elemental composition of a protoplanetary disk is assumed to be the same as for the ISM that formed the central star (Williams & Best 2014). By observing stars and interstellar clouds and estimating their elemental composition, one can make models for the protoplanetary disks, assuming that it changes slowly with time.

Protoplanetary disks are not as radiant as their central stars and cannot be observed through visual observations. However, the dust particles in the disk are hot and emit thermal radiation in a range of wavelengths from IR to sub-millimeter. This radiation can be observed and by spectroscopic analysis the dust composition can be obtained (Williams & Cieza 2011).

By combining these methods, the dust composition in protoplanetary disks is theorized to be mainly silicates and water. The fragmentation velocity is then tested in laboratories on earth for the theorized materials of the disk. Due to these experiments,  $u_f$  for the dust in a protoplanetary disk has been limited to the range:  $1 m/s \leq u_f \leq 10 m/s$  (Gundlach & Blum 2015). These values can vary throughout the disk, as various elements are condensed or vaporized. A simple calculation of this can be found in appendix B.

The dust-to-gas ratio or metallicity,  $Z$ , is difficult to observe since the gas of the disk

emit very little radiation. By the same argument as above, the dust-to-gas ratio in protoplanetary disks is assumed to be the same as for the ISM. Even the ISM dust-to-gas ratio is uncertain but constrained to about  $\sim 1/100$  (Bohlin et al. 1978). The range of metallicity used in this work is  $0.5\% \leq Z \leq 2\%$

The disk structure provided by (Bitsch et al. 2015) assumes a constant turbulent strength  $\alpha_t$  throughout the disk. As the grain size distribution input parameters comes directly from these disk structures,  $\alpha_c$  is constant in this work as well. Although an approximation, this is a common approach.

In reality,  $\alpha_t$  is actually expected to vary substantially throughout the disk, mostly in the vertical direction. The complete underlying physics behind the turbulent strength in protoplanetary disks is a current topic of discussion (Armitage 2011). One of the most important contributors to  $\alpha_t$  is the magneto rotational instability, MRI. It is a destabilizing effect that affects the orbiting charged particles in the protoplanetary disk. The charged particles moving around the central star are affected by its magnetic field. As they experience perturbations from their orbital motions, the magnetic field acts as a restoring force. This effect causes turbulence. Clearly, the MRI grows larger with the number of charged particles in the protoplanetary disk.

In the inner parts of the disk, ionization is dominated by large temperature. In the outer parts of the disk, ionization is caused by external sources such as X-rays and cosmic rays from the central star. Depending on the density of the disk, these effects mainly affect the surface layers. As  $R$  grows very large, the disk is not very dense and cosmic rays and X-rays can affect the the midplane of the disk. These effects lead to large amounts of charged particles in the inner parts of the disk, in the surface layers of the disk, and in the outer parts of the disk. Thus, the midplane of the disk at a certain range of distances has very few charged particles and therefore a low value of  $\alpha_t$ . This region is called the deadzone and can be seen clearly in figure 4.1.

A simple model of a deadzone can be found in appendix C.

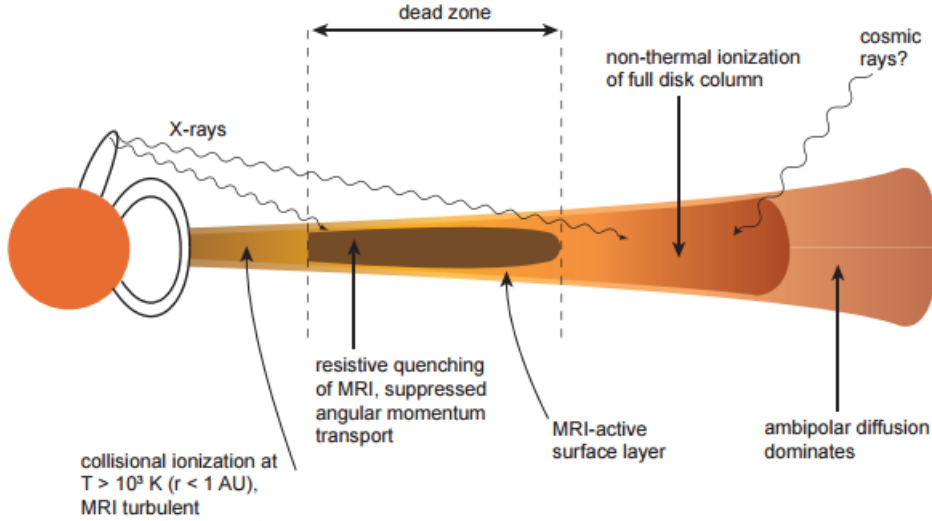


Figure 4.1: The deadzone illustrated. The dark area marked in the figure represents a lower  $\alpha_t$  due to less ionized particles. This image is taken from Armitage (2011).

The opacity has a great impact on the disk structure. It directly affects the cooling rate (equation 1.5) and determines at which depth the stellar irradiation is absorbed within the disk. A large opacity results in reduced cooling rate and thus the heat generated from the viscosity and stellar irradiation stays within the disk longer.

For inner parts of the disk the viscous heating dominates (see chapter 1). A slower cooling rate then results in increased temperature.

In the outer parts of the disk, the viscous heating is small and instead, the stellar heating dominates (see chapter 1). For most of the inner and intermediate parts of the disk, all the stellar irradiation is absorbed due to large density. Very far out, the surface density is low and the disk is not absorbing all of the stellar irradiation. Increased opacity in this part of the disk thus has a two folded effect: Increased stellar heating and decreased cooling rate, both of which leads to increased temperature.

Increased opacity thus leads to overall greater temperature while decreased opacity results in a colder disk. The temperature of the disk is one of the central structure parameters. A change in  $T$  must lead to a change in  $\Sigma$  and  $H$  in order to keep the accretion rate constant (equation 1.3). Therefore, the disk structure is highly dependent on the opacity of the disk and thus the grain size distribution.

The model presented here is a simplification of the real situation in many aspects, a few of them explained above. In addition, the simulated grain size distribution uses input parameters from the disk structure in Bitsch et al. (2015), which initially assumed an

all  $\mu m$  sized grain distribution. This clearly provides an error in the result. The model can be improved by incorporating the grain size distribution code into the disk structure simulations by Bitsch et al. (2015). This would require merging of the two codes and is beyond the scope of this work. However, The mean opacity calculated in the result section above serves as an indication of the validity of the  $\mu m$  dust size approximation in Bitsch et al. (2015). In conclusion, the  $\mu m$  dust size approximation is only valid for a very small parameter space (see figure 3.4), and thus grain size distributions has to be taken into account more carefully in future simulations.

# Chapter 5

## Appendix

### 5.1 Appendix A: Sequential growth

In the grain size distribution theory, sequential growth was assumed. This is justified below.

Assume a growth rate of a certain grain,  $m_1$ , (Barge & Pellat 1991):

$$\frac{dm_1}{dt} = \int_{m_0}^{m_1} n(m_2) m_2 C_{m_1, m_2} dm_2 \quad (5.1)$$

Taking  $\frac{m_2}{m_1} \ll 1$  and inserting equations 2.2, 2.3 and 2.4 one obtains:

$$\frac{dm_1}{dt} \propto m_1^{v-\gamma} \frac{m_1^{2+\gamma-\alpha_c} - m_0^{2+\gamma-\alpha_c}}{2 + \gamma - \alpha_c} \quad (5.2)$$

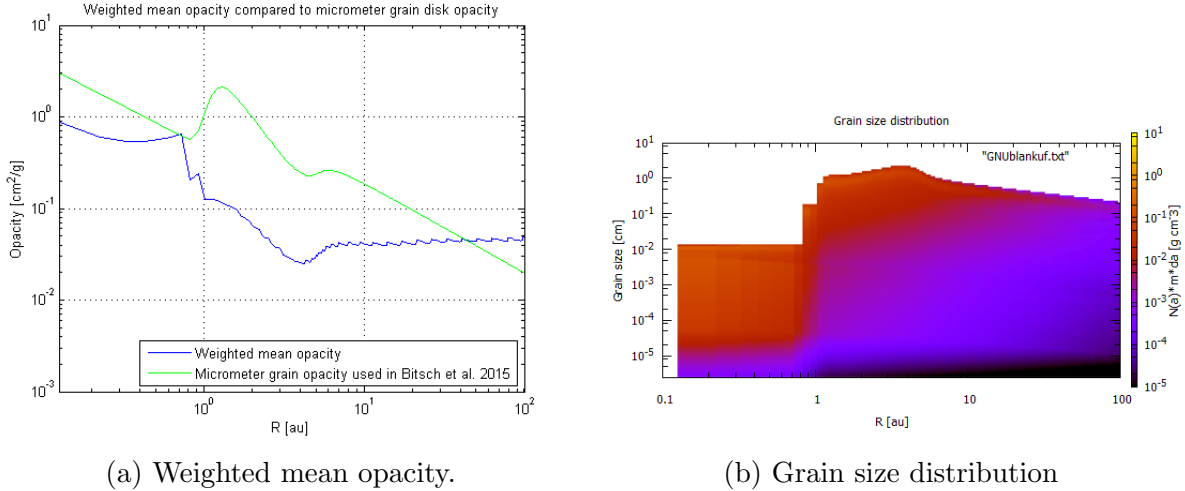
For all the  $v$  and  $\gamma$  parameters considered in Birnstiel et al. (2011) we obtain  $\alpha_c < 2 + \gamma$  and this leads to:

$$\frac{dm_1}{dt} \propto m_1^{2+v-\alpha_c} \quad (5.3)$$

This means that similarly sized grains dominates the coagulation, rather than larger grains sweeping up small grains.

## 5.2 Appendix B: Fragmentation velocity

The bump at  $R \sim 2au$  due to the ice line can be clearly seen in the opacity graph, figure 3.5. The graph features a drastic change in opacity at  $T \sim 180K$ . At this temperature the water vapor turns into solid ice particles, which contributes greatly to the disk opacity. It turns out that at  $T > 180K$  the solids of the disk are dominated by silicates, while water is in gas form. At  $T < 180K$  water condensates into ice and becomes the most dominant dust particle. Water ice and silicates have significantly different fragmentation velocities and thus  $u_f$  is expected to vary within the disk. This is not taken into account in this work. A crude treatment of the issue would be to simply set a different  $u_f$  at either side of the ice line. According to experiments made in laboratories by Gundlach & Blum (2015) on silicates and ice water, the fragmentation velocity varies by a magnitude of ten. Water ice has  $u_f \approx 10m/s$  and thus silicates has  $u_f \approx 1m/s$ . A very rough transition region between the two fragmentation velocities is implemented into the code. The result of the changing  $u_f$  can be seen in figure 5.1b. The larger  $u_f$  beyond the ice line results in larger grains. The larger grains results in lower opacity.



(a) Weighted mean opacity.

(b) Grain size distribution

Figure 5.1: Weighted mean opacity and grain size distribution of a 1 Myr disk.  $u_f = 100cm/s$  at  $T \geq 180K$  and  $u_f = 1000cm/s$  at  $T < 180K$  to simulate the difference in grain composition at either side of the ice line.  $Z = 0.5\%$  and  $\alpha_t = 0.0054$ .

The limitations of the addition to the model are obvious. First, the grains in the protoplanetary disk is a mixture of many elements rather than just silicates and water ice. There are therefore many more condensation lines where other elements transition into solid form and contribute to the opacity. Additionally, dust grains are mixtures of the solid elements in the disk, rather than solely consisting of single elements. The fragmentation velocity is therefore a more complex parameter than described here.

Second, the transition between different  $u_f$  would be very smooth in reality, as opposed to the step-by-step transition used here. For example, even though the solid water ice would

dominate beyond  $T < 180K$ , the silicates would still exist and affect the resulting  $u_f$ . The gradual transition in  $u_f$  should be taken into account in the theory of the model. However, the approximation serves as an additional understanding of the complex parameter space.

### 5.3 Appendix C: Deadzone simulation

A simple model of the horizontal (radial) deadzone is straight forward in this work since only the midplane of the disk has been considered so far. This is done by letting  $\alpha_t = 0.0054$  be the standard value of the disk. A deadzone is then introduced so that  $\alpha_t = 0.0001$  in a certain range of  $R$ . The inner limit of ionization is determined by temperature. According to Armitage (2011) the midplane of the disk contains charged particles for  $T > 1000K$ . This is the inner boundary of the deadzone. The outer boundary is given by the surface density. Cosmic rays are the most penetrating rays that cause ionization. At a certain surface density of the disk even the cosmic rays cannot penetrate to the midplane. The limit, used for this work, of  $\Sigma_g$  when ionizing cosmic rays can penetrate through to the midplane is  $\Sigma_g \sim 200g/cm^2$  from Dzyurkevich et al. (2013). These changes are implemented into the dust distribution simulation and the result is shown in figure 5.2.

As can be seen in the figure, the decreased  $\alpha_t$  in the deadzone results in significantly larger available grain sizes, locally. The rest of the grain sizes has a lower number density  $N(a)mda$  due to the normalization. This was expected from the analysis in the result section. This change in the size distribution is potentially very important for planet formation. The resulting mean opacity is displayed in figure 5.3. By the analysis provided in the result section, the mean opacity in the deadzone is decreased.  $\Sigma_g$  decreases with time which means that the deadzone outer border moves towards smaller  $R$ . This is clear from the three different epochs displayed in figure 5.2. The inner boundary of the deadzone also moves to smaller  $R$  with time due to decreasing  $T$ , but at a slower rate. Therefore the deadzone diminishes and eventually vanishes from the disk.

Note that this model of a deadzone is an oversimplification. A realistic deadzone should be included in the theory and taken into account from the start of the model. The significant vertical changes in  $\alpha_t$  should be considered.

One might conclude from the reduced opacity in the deadzone that the cooling rate would increase. An increase in cooling rate essentially causes lower temperature. However, the situation is more complicated since a lower  $\alpha_t$  means larger  $\Sigma_g$  due to the constant mass accretion (equation 1.3). By a larger  $\Sigma_g$  follows a smaller cooling rate due to equation 1.5. This is not taken into account in the model above.

Different material compositions in the disk should also result in a varying MRI and thus a varying  $\alpha_t$ . This would result in an appropriate  $\alpha_t$ -gradient in the disk. The basic model above merely outlines the basic properties of a deadzone. As can be seen in figures 5.2 and 5.3 the changing turbulent strength can have a large impact on the disk structure.

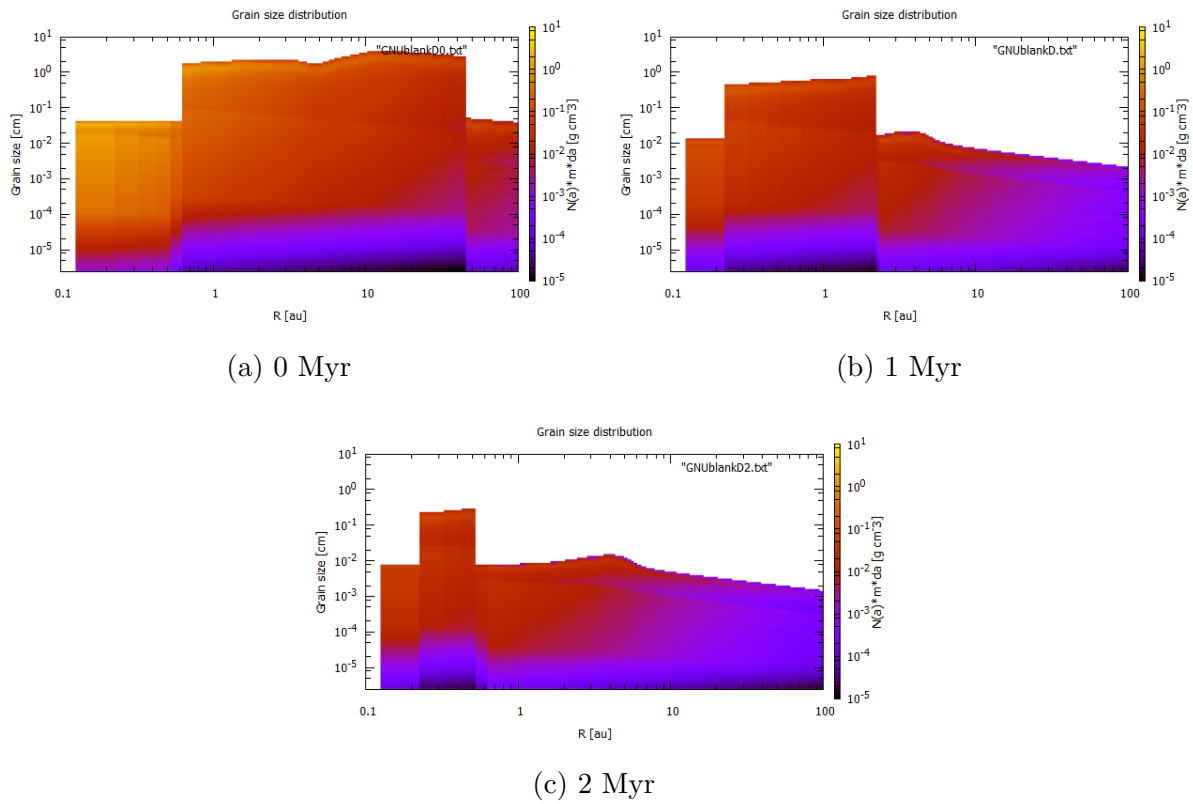


Figure 5.2: Grain size distribution over the whole disk structure (all  $R$ ) with a deadzone of  $\alpha_t = 0.0001$  included. The simulations were made with  $u_f = 100\text{cm/s}$ ,  $Z = 0.5\%$  and  $\alpha_t = 0.0054$  for three different epochs.

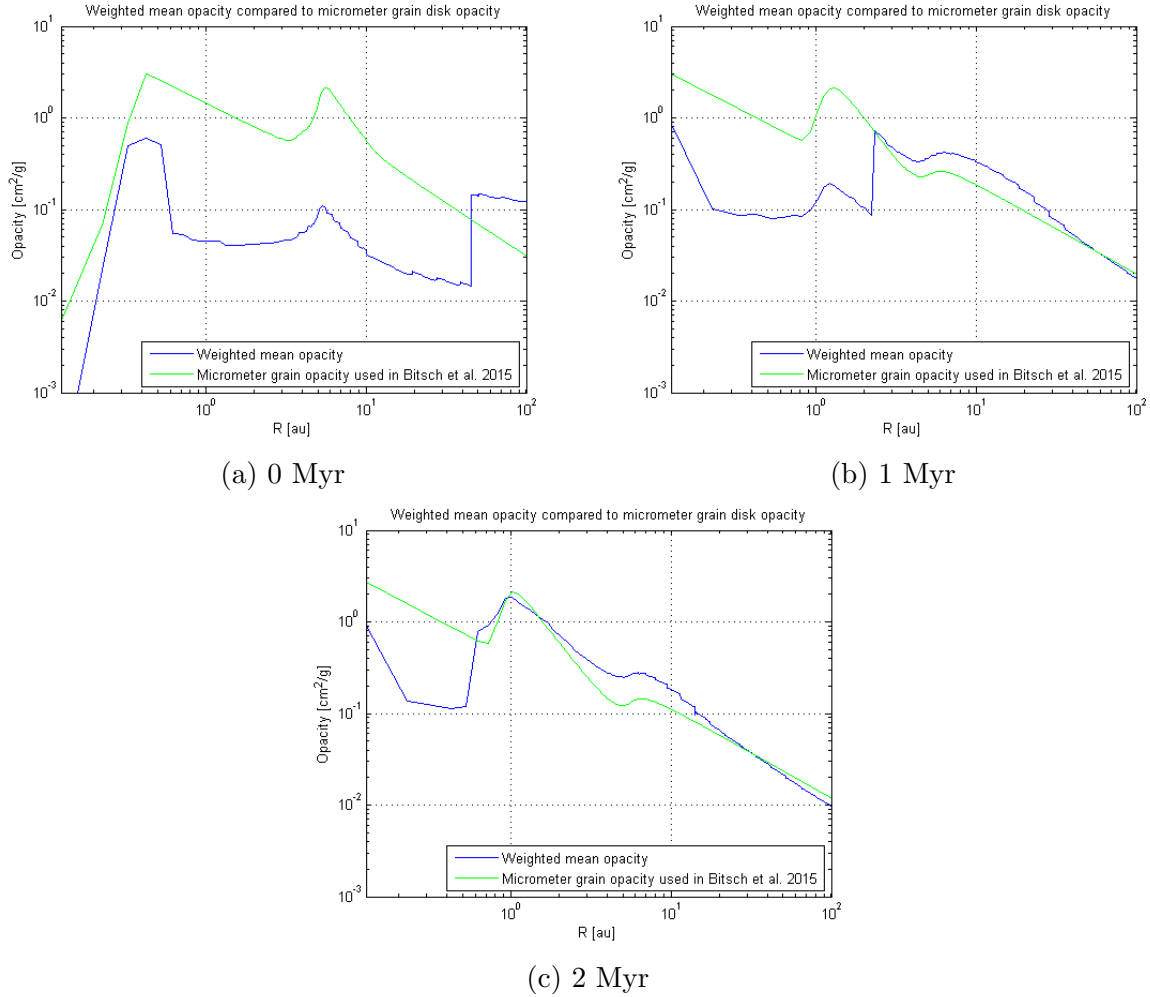


Figure 5.3: Mean opacity of the disk with a deadzone of  $\alpha_t = 0.0001$  included. The simulations were made with  $u_f = 100\text{cm/s}$ ,  $Z = 0.5\%$  and  $\alpha_t = 0.0054$  for three different epochs.

# Bibliography

- Armitage, P. J. 2011, *ARA&A*, 49, 195
- Barge, P., & Pellat, R. 1991, *Icarus*, 93, 270
- Bell, K. R., & Lin, D. N. C. 1994, *ApJ*, 427, 987
- Birnstiel, T., Andrews, S. M., Pinilla, P., & Kama, M. 2015, *ApJ*, 813, L14
- Birnstiel, T., Ormel, C. W., & Dullemond, C. P. 2011, *A&A*, 525, A11
- Bitsch, B., Johansen, A., Lambrechts, M., & Morbidelli, A. 2015, *A&A*, 575, A28
- Bitsch, B., Crida, A., Morbidelli, A., Kley, W., & Dobbs-Dixon, I. 2013, *A&A*, 549, A124
- Blum, J., & Muench, M. 1993, *Icarus*, 106, 151
- Bohlin, R. C., Savage, B. D., & Drake, J. F. 1978, *ApJ*, 224, 132
- Brauer, F., Dullemond, C. P., & Henning, T. 2008, *A&A*, 480, 859
- Davis, D. R., & Ryan, E. V. 1990, *Icarus*, 83, 156
- Dohnanyi, J. S. 1969, 74, 2531
- Dullemond, C. P. 2013
- Dullemond, C. P., & Dominik, C. 2004, *A&A*, 421, 1075
- Draine, B. T., & Lee, H. M. 1984, *ApJ*, 285, 89
- Dzyurkevich, N., Turner, N. J., Henning, T., & Kley, W. 2013, *ApJ*, 765, 114
- Fromang, S., & Nelson, R. P. 2009, *A&A*, 496, 597
- Gundlach, B., & Blum, J. 2015, *ApJ*, 798, 34
- Laike, G., Gonzalez, J.-F., & Maddison, S. T. 2012, *A&A*, 537, A61
- Makino, J., Fukushima, T., Funato, Y., & Kokubo, E. 1998, *New Astronomy*, 3, 411

- Mathis, J. S., Rumpl, W., & Nordsieck, K. H. 1977, *ApJ*, 217, 425
- Ormel, C. W., & Cuzzi, J. N. 2007, *A&A*, 466, 413
- Ormel, C. W., Paszun, D., Dominik, C., & Tielens, A. G. G. M. 2009, *A&A*, 502, 845
- Lynden-Bell, D., & Pringle, J. E. 1974, *MNRAS*, 168, 603
- Shakura, N. I., & Sunyaev, R. A. 1973, *A&A*, 24, 337
- Tanaka, H., Inaba, S., & Nakazawa, K. 1996, *Icarus*, 123, 450
- Weidenschilling, S. J. 1977, *MNRAS*, 180, 57
- Williams, J. P., & Cieza, L. A. 2011, *ARA&A*, 49, 67
- Williams, J. P., & Best, W. M. J. 2014, *ApJ*, 788, 59
- Youdin, A. N., & Lithwick, Y. 2007, *Icarus*, 192, 588